Analytic elastic coefficients in molecular calculations: Finite strain, nonaffine displacements, and many-body interatomic potentials

Jan Grießer [1], Lucas Frérot [1], Jonas A. Oldenstaedt [1], Martin H. Müser [2], and Lars Pastewka [1,3,*]

[1]*Department of Microsystems Engineering, University of Freiburg, Georges-Köhler-Allee 103, 79110 Freiburg, Germany*

[2]*Department of Material Science and Engineering, Saarland University, Campus C6 3, 66123 Saarbrücken, Germany*

[3]*Cluster of Excellence livMatS, Freiburg Center for Interactive Materials and Bioinspired Technologies, University of Freiburg, 79110 Freiburg, Germany*

Elastic moduli are among the most fundamental and important properties of solid materials, which is why they are routinely characterized in both experiments and simulations. While conceptually simple, the treatment of elastic coefficients is complicated by two factors not yet having been concurrently discussed: finite-strain and nonaffine, internal displacements. Here, we revisit the theory behind zero-temperature, finite-strain elastic moduli and extend it to explicitly consider nonaffine displacements. We further present analytical expressions for second-order derivatives of the potential energy for two-body and generic many-body interatomic potentials, such as cluster and empirical bond-order potentials. Specifically, we revisit the elastic constants of silicon, silicon carbide, and silicon dioxide under hydrostatic compression and dilatation. Based on existing and recent results, we outline the effect of multiaxial stress states as opposed to volumetric deformation on the limits of stability of their crystalline lattices.

I. INTRODUCTION

Elastic constants, also known by the better terms elastic moduli or *elastic coefficients*, describe the stress needed to reversibly strain a solid. If the solid is already strained, they correspond to the extra stress needed to deform it further. Elastic coefficients are among the most fundamental and important properties of solids and are hence routinely computed in atomic-scale calculations. Unfortunately, a rigorous computation of these deceivingly simple properties is complicated by two factors. First, neither stress nor strain are uniquely defined [1,2], except in the immediate vicinity of zero external stress, so numerous definitions of elastic tensors exist. Which of the various definitions of finite-strain elastic coefficients matters depends on the property of interest. For example, the elastic tensors used to deduce the generally polarization- and direction-dependent sound velocity [3–6] are different from those used to analyze lattice stability [6–15], which, according to Born, necessitates the elastic tensor to be positive definite. Second, atomic positions undergo nonaffine internal relaxations in response to a macroscopic shape change, except in the case of highly symmetric crystals for which all Wykoff positions are fully determined by symmetry even in the deformed state [16]. An extreme case for solids with nonaffine

internal relaxations are amorphous materials for which no single atomic position can be deduced from symmetry.

While the effect of thermal fluctuations on elastic coefficients has become text-book material [17], we are not aware of similarly comprehensive, let alone comprehensible works on the interplay of elastic coefficients and finite stress. For example, we do not know of any prior work clearly illustrating the existence and uniqueness of the generalization of the enthalpy or Gibb's free energy when a nonisotropic external stress is applied. Moreover, a fast and numerically stable evaluation of elastic coefficients based on second-order derivatives of the potential has so far been achieved only for a rather limited class of potentials, see, e.g., Ref. [[17], Chap. 11.5.2] and Refs. [18–24]. The derivations in these works pertain to fixed, specific functional forms prohibiting results to be transferred between different functional forms.

The purpose of this paper is to further finite-strain elasticity in the presence of external stresses and nonaffine displacements. To this end, we first revisit definitions of strain and stress and their relation to thermodynamic potentials in Sec. II. This includes a discussion of how the Gibbs free energy can be properly generalized when the stress is not isotropic. Moreover, elastic tensors are introduced as second-order derivatives of thermodynamic potentials and the Born-stability criteria are reassessed, after the determination of finite-strain, nonaffine displacements was generalized with a variational formulation inspired by (continuum) stochastic homogenization techniques. A unified treatment for calculating stress and elastic tensor elements is derived in Sec. III. It exploits a recently suggested generic functional form containing various interaction potentials, such as the embedded-atom method, Stillinger-Weber, Tersoff-Brenner, Axilrod-Teller-Muto, and

cluster potentials [25]. The corresponding software implementation is available within the open-source MATSCIPY library [26]. After introducing numerical methods in Sec. IV, we explore the lattice stability of silicon, silicon carbide, and silicon dioxide crystals under hydrostatic and multiaxial stress in Sec. V and conclude in Sec. VII.

II. FINITE DEFORMATION AND THERMODYNAMIC POTENTIALS

A. Finite strain

To arrive at a self-contained treatise, we begin by revisiting and summarizing part of the pertinent literature on finite-strain elasticity. A more detailed presentation is given in Ref. [17], which will be referred to throughout this paper. We assume a periodic simulation cell in D dimensions, which can also serve as a representative volume element (RVE). Its geometry is described by the h matrix [27], $\underline{h} \equiv (\vec{a}_1, \ldots, \vec{a}_D)$, whose D columns $\vec{a}_i$ are D-dimensional vectors spanning the simulation cell. The volume of the simulation cell is then given by $V = \det(\underline{h})$. Positions of atoms in the simulation cell can be stated in terms of either true coordinates, $\vec{r}_i$, or unitless, scaled coordinates, $\vec{s}_i$. True and scaled coordinates of the $i = 1, \ldots, N$ atoms in the simulation cell are related through the equation $\vec{r}_i = \underline{h} \cdot \vec{s}_i$.

Let us define one particular h matrix as the reference h matrix and indicate its reference status with a circle as $\overset{\circ}{\underline{h}}$. Similarly, we assume reference scaled atomic coordinates, $\overset{\circ}{\vec{s}}_i$. The effect of an *affine* deformation of the simulation cell can be described by the *deformation gradient* $\underline{F}$ acting on the reference cell according to $\underline{h} = \underline{F} \cdot \overset{\circ}{\underline{h}}$ while leaving the $\overset{\circ}{\vec{s}}_i$ unchanged, $\vec{s}_i \equiv \overset{\circ}{\vec{s}}_i$. In the affinely deformed cell, atomic coordinates thus read

$$\underline{r}_i = \underline{F} \cdot \overset{\circ}{\vec{r}}_i \quad \text{or} \quad r_{i\alpha} = F_{\alpha\beta} \overset{\circ}{r}_{i\beta}, \tag{1}$$

where $\overset{\circ}{\vec{r}}_i = \overset{\circ}{\underline{h}} \cdot \overset{\circ}{\vec{s}}_i$. We have written Eq. (1) in tensor and index notation and use Einstein summation convention for repeated indices in the latter. Atoms are identified by Roman indices, directions by Greek indices. In tensor notation, there are no Greek indices but an arrow indicates a D-vector and an underline a $D \times D$-matrix. We will switch between tensor and index notation throughout this paper, using the notation that we deem appropriate for each equation.

In the absence of external (magnetic, electric, or strong gravitational) fields, the potential energy is translationally and rotationally invariant, a property that is called *objectivity* in the field of mechanics. The total potential energy of a system can then only depend on the set of distances $r_{ij} = |\vec{r}_i - \vec{r}_j|$ rather than on the absolute positions. This is also true for potentials beyond the pair-potential approximation, since knowledge of all r_{ij} defines the system up to translation, rotation, and handedness.

It is important to note that absolute distances transform as $R_{ij} \equiv r_{ij}^2 = \overset{\circ}{\vec{r}}_{ij} \cdot \underline{F}^T \cdot \underline{F} \cdot \overset{\circ}{\vec{r}}_{ij}$, with the *right Cauchy–Green deformation tensor* $\underline{F}^T \cdot \underline{F}$. The *strain* in the system is often characterized by how much this deformation tensor deviates from the identity matrix, $\underline{1}$, giving the *Green–Lagrange strain*

tensor [28]:

$$\underline{\eta} \equiv \tfrac{1}{2}(\underline{F}^T \cdot \underline{F} - \underline{1}). \tag{2}$$

The Green–Lagrange strain is sometimes denoted by the symbol $\underline{E}$ in the solid mechanics literature.

We can write the deformation gradient in terms of the h matrix as

$$\underline{F} = \underline{h} \cdot \overset{\circ}{\underline{h}}{}^{-1}.$$

The Green–Lagrange strain tensor then becomes

$$\underline{\eta} = \tfrac{1}{2}(\overset{\circ}{\underline{h}}{}^{-T} \cdot \underline{h}^T \cdot \underline{h} \cdot \overset{\circ}{\underline{h}}{}^{-1} - \underline{1}). \tag{3}$$

The Green–Lagrange strain tensor is hence *always* defined with respect to a reference h matrix. Moreover, the Green-Lagrange strain tensor is independent of rotation, that is, $\underline{\eta}$ remains unchanged upon rotation of the simulation cell. This can be seen when rotating each vector spanning the $\underline{h}$ matrix in Eq. (3) through the operation $\underline{R} \cdot \underline{h}$, where $\underline{R}$ is a rotation matrix fulfilling $\underline{R}^T \cdot \underline{R} = \underline{1}$.

Another measure for the deformation is the small–strain tensor [28]

$$\underline{\varepsilon} \equiv \tfrac{1}{2}(\underline{F} + \underline{F}^T) - \underline{1}, \tag{4}$$

which does not remain unchanged under a rotation of the h matrix. Finally, for symmetric $\underline{F} = \underline{1} + \underline{\varepsilon}$,

$$\eta_{\alpha\beta} = \varepsilon_{\alpha\beta} + \tfrac{1}{2}\varepsilon_{\alpha\gamma}\varepsilon_{\gamma\beta},$$

from which the partial derivative of $\eta_{\alpha\beta}$ with respect to $\varepsilon_{\mu\nu}$ can be obtained as

$$\frac{\partial \eta_{\alpha\beta}}{\partial \varepsilon_{\mu\nu}} = \delta_{\alpha\mu}\delta_{\beta\nu} + \frac{1}{2}(\delta_{\alpha\mu}\varepsilon_{\nu\beta} + \varepsilon_{\alpha\mu}\delta_{\beta\nu}).$$

Thus, for a second-order derivative of an arbitrary function f, the following chain-rule applies:

$$\frac{\partial^2 f}{\partial \varepsilon_{\alpha\beta} \partial \varepsilon_{\mu\nu}}\bigg|_{\underline{\varepsilon}=0} = \frac{\partial^2 f}{\partial \eta_{\alpha\beta} \partial \eta_{\mu\nu}}\bigg|_{\underline{\eta}=0} + \frac{\partial f}{\partial \eta_{\alpha\mu}}\bigg|_{\underline{\eta}=0} \delta_{\beta\nu}.$$

B. Internal and free energy

Assuming the initial structure to be fully relaxed mechanically, we define a zero-temperature energy

$$U(N, \underline{h}) = \min_{\{\vec{s}_i\}} u(\{\vec{s}_i\}, \underline{h}),$$

where $U(N, \underline{h})$ is the internal energy. Here, the minimization is meant to implicitly contain the instruction "next available minimum" along an adiabatic change of the h matrix from $\overset{\circ}{\underline{h}}$ to $\underline{h}$. Unlike for a global minimum, this means that $U(N, \underline{h})$ depends on the atomic coordinates in the initial reference configuration and on the path from $\overset{\circ}{\underline{h}}$ to $\underline{h}$.

In a thermal (equilibrium) system, the instantaneous energy has to be replaced with the Helmholtz free energy A, which would be the proper thermodynamic potential that the internal coordinates would minimize in thermal equilibrium at the fixed h matrix. For a classical, single-atomic system, it is formally defined as

$$A(N, T, \underline{h}) = -k_B T \ln Z(N, T, \underline{h}),$$

with

$$Z(N, T, \underline{h}) = \frac{1}{N!} \frac{1}{\lambda_B^{3N}} \int d\Gamma_c e^{-u(\Gamma_c, \underline{h})/(k_B T)}. \quad (5)$$

General phase-space averages of an observable O are given by

$$\langle O \rangle = Z^{-1} \int d\Gamma_c O(\Gamma_c, \underline{h}) e^{-u(\Gamma_c, \underline{h})/(k_B T)}. \quad (6)$$

Here $k_B T$ is the thermal energy and λ_B the de Broglie wavelength, while Γ_c represents the configurational phase space containing all Cartesian coordinates of the N atoms, which are confined to the volume spanned by the h matrix.

When defining an elastic free energy of solids, it is generally necessary to constrain the phase-space integral in Eqs. (5) and (6), since otherwise even macroscopic crystals would lose their ability to withstand nonisotropic stress and consequently fill any volume in a similar fashion as liquids do. This is because in true equilibrium, solids can release static stress over long timescales, e.g., through the motion of lattice defects like vacancies or dislocations. Thus, in the above definition of the free energy, it is necessary to keep in mind the concept of the separation of timescales and to restrict the integration over phase space to only those configurations that can be reached from the initial or reference configuration without having to pass over (macroscopically) large energy barriers, as those configurations are not reached by thermal fluctuations on an experimental timescale. Alternatively, one could conduct the phase-space integration within the harmonic approximation, or restrict the integral to the configurations having fixed bonding topography, or to basins in which the Hessian of the energy with respect to (scaled) atomic coordinates is positive definite. This then necessitates the introduction of additional collective variables describing the current local minimum for which to compute the free energy. Ultimately, a certain ambiguity for the definition of a meaningful restricted free energy remains. However, the supposedly justified hope is that final results do not vary much between sensitive choices of the restriction.

To make the definition of an elastic free energy at finite temperature more concrete, we constrain mean atomic positions of individual atoms, $\langle \vec{s}_i \rangle$ to $\vec{s}_i^c$ [29], and choose $\vec{s}_i^c$ such that the constraint free energy, $a(\{\vec{s}_i^c\}; \underline{h})$, is minimized. In a purely harmonic solid, the $\vec{s}_i^c$ are the equilibrium positions at zero temperature, but not generally in anharmonic solids. At zero temperature, this free energy reduces to the internal energy. In the following, we drop the explicit superscript c from the equations, and implicitly refer to the constraint variables when writing $\vec{s}_i$ or $\vec{r}_i$. To conclude, we assume not only the internal but also the free energy to depend on some (initial) reference configuration and provide definitions for any arbitrary h matrix, including those where a given h matrix is a strained configuration.

C. Stresses as conjugates to strain variables

Stresses can be defined as the first-order derivative of the free energy with respect to a strain measure. This leaves different stress tensors to be defined because different strain tensors exist. Formally, the stress for an arbitrary structure is given by

$$\underline{\sigma}^{\eta} \equiv \frac{1}{V} \frac{\partial A(\{\vec{s}_i\}, \underline{h})}{\partial \underline{\eta}}, \quad (7)$$

where the derivative is to be interpreted componentwise (i.e., it is the gradient). Internal relaxation of the atomic coordinates during the small perturbation of the cell necessary to compute the derivative do not matter if the $\vec{s}_i$ minimize the free energy for the cell $\underline{h}$, which we will assume in the following. Relaxation only matters at second order and will affect the elastic constants discussed below.

The stresses obtained from Eq. (7) differ for different strain measures unless they are evaluated at zero strain. The nomenclature that was implicitly introduced uses upper indices to indicate the definition of the stress, i.e., the strain tensor with respect to which the first-order derivative of the free energy was taken. At this point, we abstain from associating pertinent expressions with the commonly used names, which are Kirchhoff, nominal, first and second Piola–Kirchhoff, and Biot stress [28].

D. Generalized Gibbs free energy

In thermodynamics, coupling a subsystem to an external bath is commonly done such that at least one extrinsic thermodynamic variable associated with the subsystem, e.g., the particle number N, is kept constant and at least one is relaxed, such as volume V, while its conjugate variable, in this case the hydrostatic pressure p, is constrained to a fixed value. In this specific example, the *extended* Gibbs free energy,

$$g(N, p, T; V) = A(N, V, T) + pV, \quad (8)$$

would then be minimized with respect to the volume V yielding the Gibbs free energy:

$$G(N, p, T) = \min_V g(N, p, T; V). \quad (9)$$

The value of V minimizing $g(N, p, T; V)$, V^{eq}, is the expectation or equilibrium value of the volume. Note that Eq. (9) has formally the form of a Legendre transformation. Rather than stating V^{eq} as a function of p, it is common to express pressure as a function of V^{eq}, i.e.,

$$p \equiv p(V^{eq}) = -\left. \frac{\partial A}{\partial V} \right|_{V^{eq}},$$

which follows from the requirement that V minimizes the extended Gibb's free energy in Eq. (8) at $V = V^{eq}$.

A physical realization of the just-described situation could be a crystal—for the sake of simplicity described within the harmonic approximation to avoid discussions related to broken ergodicity or separation of timescales—embedded into an ideal gas, which acts as an infinitely large bath while exerting the pressure p on the crystal. The term $W = pV$ is the work done on the gas to make room for the crystal or, alternatively, the work done on the periodic boundary conditions imposed in a molecular simulation. In the following, we will not distinguish between these two cases so the h matrix can be said to span our subsystem, which thus is implicitly assumed to be a parallelepiped.

The gas can freely flow around our crystal, thus imposing purely hydrostatic conditions. Unfortunately, it is not possible to construct a related expression for the work imposing a constant nonisotropic stress (which cannot be realized by an ideal gas as an embedding medium) that would be independent of the current h matrix. A general path-independent work has to

be a function of the h matrix so the most general extended Gibbs free energy reads

$$g(\underline{h}) = A(\underline{h}) + W(\underline{h}), \tag{10}$$

with the hydrodynamic case leading to the special choice of $W(\underline{h}) = p \det(\underline{h})$. Before proceeding, we note that $g(\underline{h})$ can depend on many more variables than just N, T, which were dropped in the discussion.

One (formally) possible dependence of the work on $\underline{h}$ would be

$$W = -\Pi_{11} h_{11} \mathring{h}_{22} \mathring{h}_{33} - \Pi_{22} \mathring{h}_{11} h_{22} \mathring{h}_{33} - \Pi_{33} \mathring{h}_{11} \mathring{h}_{22} h_{33}, \tag{11}$$

and the parameters $\Pi_{\alpha\beta}$ could be associated with the coefficients of a target stress tensor. Minimizing Eq. (10) yields the equilibrium h matrix $\underline{h}^{\text{eq}}$. For $\mathring{\underline{h}} = \underline{h}^{\text{eq}}$, $\underline{\Pi}$ can be associated with the externally imposed stress, which does not have to be isotropic. Thus, to impose the three desired independent stress-tensor eigenvalues of a symmetric stress tensor in a molecular simulation using Eq. (11), it is necessary to know ahead of time or, alternatively, to identify by recursion the equilibrium h matrix [30]. Any deviation of $\mathring{\underline{h}}$ from $\underline{h}^{\text{eq}}$ will generally make the actual stress acting on the subsystem deviate from the target stress. Note, however, that we can always interpret $\underline{\Pi}$ as the stress acting in some reference configuration with h-matrix $\underline{h}$. This type of stress is commonly called the second Piola-Kirchhoff stress, as opposed to the true or Cauchy stress that acts in the equilibrium configuration.

It can be helpful to realize that imposing a constant, isotropic stress using Eq. (11) will lead to different thermal fluctuations of the h matrix—and thus to different stability conditions—than if the isotropic stress were imposed through $W = p \det \underline{h}$. Both are determined by a second-order expansion of g into h matrix elements. It may be concluded that individual stress tensor elements cannot be used as independent, intrinsic thermodynamic variables. The stress acting on the surface of a subsystem embedded into an elastic medium (the bath), say, an ideal, heterogeneous but anisotropic linearly elastic manifold, is not necessarily identical to that associated with a spatial average over the embedding medium. Equilibrium merely requires $\nabla \cdot \underline{\sigma}$ to vanish. In other words, the (equilibrium) bath stress is not necessarily the one acting on the surface of the subsystem. Even worse, in a real subsystem/bath system, the subsystem would generally not maintain the shape of a parallelepiped, due to stress singularities near the edges and corners if subsystem and embedding differ in their elastic properties. Any constant stress ensemble must therefore make a simplifying assumption and rely on a hypothetical stress boundary condition, which is unlikely representative of the true situation.

To connect back to solid mechanics, we rewrite the thermodynamic potentials in terms of a strain and a reference h matrix, $\mathring{\underline{h}}$. Working with strain has the advantage that W can be made objective. This eliminates degeneracy in the thermodynamic potentials, but at the cost of introducing some (artificial) reference $\mathring{\underline{h}}$, which has no specific physical meaning unless chosen at zero stress. A linear expansion of W in η yields

$$W = -\mathring{V}(\Pi_{11} \eta_{11} + \Pi_{22} \eta_{22} + \Pi_{33} \eta_{33}), \tag{12}$$

with $\mathring{V} = \det \mathring{\underline{h}}$, but this expression only corresponds to Eq. (11) to linear order.

E. Work on a hypothetical embedding medium

To generalize the above discussion to nonorthorhombic deformation, described by some parameterized configuration path $\underline{h}(s)$, or $\underline{\eta}(s)$, we adopt a continuum view on our RVE. Specifically, our goal is to homogenize the response of the molecular RVE to that of an equivalent homogeneous elastic continuum. This implies that the deformation throughout the *homogenized* RVE is affine. (For this discussion, it does not matter that the deformation in our reference molecular RVE, as discussed below, will be nonaffine.)

We now compute the work W performed on the embedding medium along some parameterized path s at hypothetical constant external stress $\underline{\tau}$. Note that s can be interpreted as a form of time, in which case derivatives with respect to s becomes rates and we will denote such derivatives with a dot, $\dot{W} = dW/ds$. As already discussed above, we call this embedding medium "hypothetical", because we ignore boundary effects that may arise from a mismatch of elastic properties between embedding medium and RVE. We also ignore stress gradients that may be present in the embedding medium, depending on the macroscopic (at infinity) boundary conditions. This hypothetical embedding medium can be imagined as consisting of infinitely repeated images of the RVE under perfectly matched boundary conditions.

Assuming that the current configuration of the RVE has h matrix $\underline{h}(s)$, the work W performed on the embedding medium along an arbitrary path s is given by

$$W = \int dW = \int ds \, \dot{W} \tag{13}$$

where $\dot{W}$ is the power that is obtained by integrating the external forces $d\vec{f}(\vec{r}) = -\underline{\tau} \cdot \hat{n}(\vec{r}) d^2 r$ times the velocity $\dot{\vec{u}}$ over the surface $\partial \underline{h}$ of our RVE. To simplify our notation we omit the explicit dependency on $\vec{r}$ for the remaining part of this section. The rate of work $\dot{W}$ is

$$\dot{W} = \int d\vec{f} \cdot \dot{\vec{u}} = -\int_{\partial \underline{h}(s)} d^2 r \, \dot{\vec{u}} \cdot \underline{\tau} \cdot \hat{n},$$

where $\hat{n}$ is the normal vector of the surface. The tensor $\underline{\tau}$ is symmetric because of conservation of angular momentum.

Let us now assume that we have a Cauchy stress field $\underline{\sigma}$ throughout the RVE. On the boundary $\underline{\sigma} = \underline{\tau}$. We remain at mechanical equilibrium where $\nabla \cdot \underline{\sigma} = 0$ along the deformation path. To relate $\underline{\sigma}$ to the rate of work of external forces, we use the divergence theorem:

$$\dot{W} = -\int_{\partial \underline{h}(s)} d^2 r \, \dot{\vec{u}} \cdot \underline{\sigma} \cdot \hat{n} = -\int_{\underline{h}(s)} d^3 r \, \nabla \cdot [\underline{\sigma} \cdot \dot{\vec{u}}].$$

Under mechanical equilibrium, this yields

$$\dot{W} = -\int_{\underline{h}(s)} d^3 r \, \underline{\sigma} : \nabla \dot{\vec{u}} = -\int_{\underline{h}(s)} d^3 r \, \underline{\sigma} : \dot{\underline{\varepsilon}}, \tag{14}$$

where $\dot{\underline{\varepsilon}}$ is the strain-rate tensor. The colon indicates a double contraction, that is, $\underline{A} : \underline{B} = A_{\alpha\beta} B_{\beta\alpha}$. The integral in Eq. (14) is over the current configuration.

The tensor $\dot{\underline{\varepsilon}}$ is defined with respect to the current h matrix $\underline{h}(s)$ along the deformation path. We cannot directly evaluate the integral Eq. (13), because the h matrix (which enters the integration bounds) depends on s in Eq. (14). By introducing a reference h matrix $\underline{\mathring{h}}$ and reference coordinates $\vec{\mathring{r}}$, we can express the velocity by $\dot{\vec{u}}(s) = \dot{\underline{F}}(s) \cdot \vec{\mathring{r}} = \dot{\underline{F}}(s) \cdot \underline{F}^{-1}(s) \cdot \vec{r}(s)$, where $\dot{\underline{F}}$ is the rate of change of the deformation gradient $\underline{F}$. This yields

$$\dot{\underline{\varepsilon}} = \frac{1}{2}\left[\frac{\partial \dot{\vec{u}}}{\partial \vec{r}} + \left(\frac{\partial \dot{\vec{u}}}{\partial \vec{r}}\right)^T\right] = \frac{1}{2}(\dot{\underline{F}} \cdot \underline{F}^{-1} + \underline{F}^{-T} \cdot \dot{\underline{F}}^T).$$

From Eq. (2), we get

$$\dot{\underline{\eta}} = \tfrac{1}{2}(\dot{\underline{F}}^T \cdot \underline{F} + \underline{F}^T \cdot \dot{\underline{F}}),$$

which we can use to write the power as a first-order expression in s,

$$\dot{W} = -\int_{\underline{\mathring{h}}} d^3\mathring{r}\, \underline{\Pi} : \dot{\underline{\eta}}, \tag{15}$$

where the integral is now over our (arbitrarily chosen) reference cell with h matrix $\underline{\mathring{h}}$. Note we have identified

$$\underline{\Pi} \equiv J\underline{F}^{-1} \cdot \underline{\sigma} \cdot \underline{F}^{-T}, \tag{16}$$

with $J = \det \underline{F}$. Equation (16), which is often referred to as a pull-back operation [17,28,31,32], transforms the true (or Cauchy) stress $\underline{\sigma}$ into the second Piola–Kirchhoff stress $\underline{\Pi}$. Identical expressions have been derived in the context of lattice stability [13,14] and constant pressure molecular dynamics simulations [30].

F. Finite-strain elastic coefficients

We now assume that the RVE can be described by an equivalent homogeneous elastic continuum, which can only deform affinely. Then $\dot{\underline{\eta}}$ is constant throughout the RVE and equivalent to the applied macroscopic strain. This means we can replace $\underline{\Pi}(\vec{r})$ in Eq. (15) by its spatial average $\underline{\Pi}$. Integration yields

$$W = -\int_{s_0}^{s_1} ds \int_{\underline{\mathring{h}}} d^3\mathring{r}\, \underline{\Pi} : \dot{\underline{\eta}} = -\mathring{V}\,\underline{\Pi} : \underline{\eta},$$

where η is the total strain along path $s_0 \to s_1$. This gives our *ad hoc* Eq. (12) in the orthorhombic case. The Gibbs free energy, in analogy to Eq. (9), for arbitrary cell deformation is then

$$G(\underline{\Pi}; \underline{\mathring{h}}) = \min_{\underline{\eta}} g(\underline{\Pi}; \underline{\mathring{h}}; \underline{\eta}),$$

$$g(\underline{\Pi}; \underline{\mathring{h}}; \underline{\eta}) = A(\underline{\mathring{h}}; \underline{\eta}) - \mathring{V}\,\underline{\Pi} : \underline{\eta}, \tag{17}$$

where $\eta = 0$ is some reference configuration with h matrix h [see Fig. 1(a)], which is not necessarily in mechanical equilibrium [see Fig. 1(b)]. The quantity $g(\underline{\Pi}; \underline{\mathring{h}}; \underline{\eta})$ is the extended Gibbs free energy of a (small) system at strain $\underline{\eta}$.

We now strain the system against the constant external stress $\underline{\Pi}$ of a surrounding embedding medium [Fig. 1(c)]. The
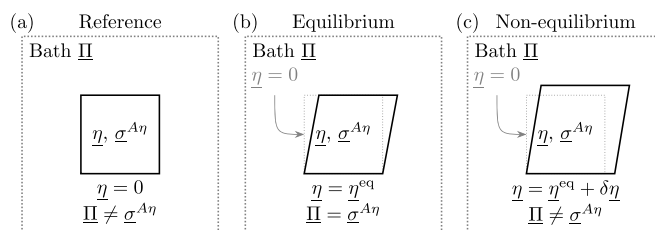
FIG. 1. Thermodynamics of elastic deformation. The external stress $\underline{\Pi}$ is a property of a hypothetical ideal embedding medium. Equilibrium is the case where embedding medium and system pressure are equal, $\underline{\Pi} = \underline{\sigma}^\eta$. (a) Our reference configuration is not necessarily at equilibrium. (b) Equilibrium is obtained at some finite strain η^{eq} where bath and system pressure are equal. (c) We make small deformations around this equilibrium condition to probe the elastic properties of the system at constant stress $\underline{\Pi}$.

equilibrium condition for the strain yields

$$\left.\frac{\partial g}{\partial \underline{\eta}}\right|_{\underline{\eta}^{\mathrm{eq}}} = 0 \quad \text{or} \quad \underline{\Pi} = \frac{1}{\mathring{V}}\left.\frac{\partial A}{\partial \underline{\eta}}\right|_{\underline{\eta}^{\mathrm{eq}}} \equiv \underline{\sigma}^\eta(\underline{\mathring{h}}; \underline{\eta}^{\mathrm{eq}}), \tag{18}$$

which lets us identify $\underline{\Pi}$ as the conjugate to the Green–Lagrange strain $\underline{\eta}$, so $\underline{\Pi}$ has the properties of a second Piola–Kirchhoff stress. It is important to emphasize that $\underline{\Pi}$ is a property of the embedding medium while $\underline{\sigma}^\eta$ is a property of the system, and that equilibrium requires $\underline{\Pi} = \underline{\sigma}^\eta$, see Fig. 1(b). Eqs. (17) and (18) depend parametrically on the reference configuration $\underline{\mathring{h}}$, as the strain $\underline{\eta}$ is defined with respect to this reference [see Figs. 1(a) and 1(b)]. Of course, this equilibrium is constrained by the conditions described in Sec. II D, in particular, that the cell remains a parallelepiped.

We can remove the choice of an arbitrary reference state in Eq. (18) by choosing the h matrix that corresponds to $\underline{\eta}^{\mathrm{eq}}$ as our new reference $\underline{\mathring{h}}$. For this choice, $\eta^{\mathrm{eq}} = 0$. The explicit dependence on η^{eq} in Eq. (18) then disappears, and we can write

$$\underline{\Pi}(\underline{\mathring{h}}) = \frac{1}{\mathring{V}}\left.\frac{\partial A}{\partial \underline{\eta}}\right|_{\underline{\eta}=0}.$$

This corresponds to how we typically estimate stresses in molecular calculations: We pick an h matrix $\underline{\mathring{h}}$ and then perform small perturbations of the cell to determine the stress.

The derivative $\partial g/\partial \underline{\eta}$ must be a monotonously increasing function passing through zero at $\eta^{\mathrm{eq}} \equiv 0$. Loss of monotonous increase of this function means loss of convexity of the extended Gibbs free energy, and hence loss of (mechanical) stability. We *define* the elastic coefficients $\underline{\underline{c}}$ as the second derivative of the extended Gibbs free energy

$$\underline{\underline{c}}^\Pi(\underline{\Pi}; \underline{\mathring{h}}) \equiv \frac{1}{\mathring{V}}\left.\frac{\partial^2 g}{\partial \underline{\eta}^2}\right|_{\underline{\eta}=0},$$

where the superscript on the elastic coefficient tensor $\underline{\underline{c}}$ indicates the stress that was held constant. Evaluating the elastic

coefficients at constant $\underline{\Pi}$ yields

$$\underline{\underline{c}}^{\Pi} = \frac{1}{\mathring{V}} \left. \frac{\partial^2 A}{\partial \underline{\eta}^2} \right|_{\underline{\eta}=0} = \left. \frac{\partial \underline{\sigma}^{\eta}}{\partial \underline{\eta}} \right|_{\underline{\eta}=0}.$$

This expression shows directly that the elastic coefficients are the second derivative of the free energy – an expression that we might have written down intuitively and that is often the starting point in related works. Note that we can similarly *define*

$$\underline{\underline{c}}' = \frac{1}{\mathring{V}} \left. \frac{\partial^2 A}{\partial \underline{\varepsilon}^2} \right|_{\underline{\varepsilon}=0}, \tag{19}$$

but this elastic tensor does not equal $\underline{\underline{c}}^{\Pi}$. Eq. (4) can be used to relate $\underline{\eta}$ and $\underline{\varepsilon}$:

$$c'_{\alpha\beta\mu\nu} = c^{\Pi}_{\alpha\beta\mu\nu} + \sigma_{\alpha\mu}\delta_{\beta\nu}.$$

Conceptually, we made small deformations of the equilibrium configuration and measure the resulting changes in stress [see Fig. 1(c)] at constant second Piola–Kirchhoff stress $\underline{\Pi}$. We are often interested in an embedding medium that sustains a constant Cauchy rather than Piola-Kirchhoff stress. We use Eq. (15) and the pull-back Eq. (16) to write the deviation of the extended Gibbs free energy from equilibrium as

$$\delta g = \delta A - \mathring{V} J (\underline{F}^{-1} \cdot \underline{\sigma} \cdot \underline{F}^{-T}) : \delta\underline{\eta}. \tag{20}$$

Unfortunately, this equation is not a differential, i.e., we cannot write a potential g that yields Eq. (20) as a derivative. This is most easily seen by computing the elastic coefficients at constant Cauchy stress:

$$c^{\sigma}_{\alpha\beta\mu\nu} = \frac{1}{\mathring{V}} \frac{\partial}{\partial\eta_{\alpha\beta}} \left. \frac{\delta g}{\delta\eta_{\mu\nu}} \right|_{\underline{\eta}=0}$$
$$= c^{\Pi}_{\alpha\beta\mu\nu} - \sigma_{\alpha\beta}\delta_{\mu\nu} + \sigma_{\beta\nu}\delta_{\alpha\mu} + \sigma_{\alpha\nu}\delta_{\beta\mu}. \tag{21}$$

Because $\underline{\eta}$ is symmetric, $\eta_{\alpha\beta} \equiv \eta_{\beta\alpha}$ for $\alpha \neq \beta$, we can symmetrize Eq. (21) with respect to $\mu \leftrightarrow \nu$ (it is already symmetric in $\alpha \leftrightarrow \beta$), yielding

$$c^{\sigma}_{\alpha\beta\mu\nu} = c^{\Pi}_{\alpha\beta\mu\nu} + \tfrac{1}{2}(\sigma_{\alpha\mu}\delta_{\beta\nu} + \sigma_{\alpha\nu}\delta_{\beta\mu} + \sigma_{\beta\mu}\delta_{\alpha\nu}$$
$$+ \sigma_{\beta\nu}\delta_{\alpha\mu} - 2\sigma_{\alpha\beta}\delta_{\mu\nu}). \tag{22}$$

If the elastic coefficients were given as the second derivative of a thermodynamic potential, then by virtue of the symmetry of second derivatives (Schwarz theorem), they must fulfill Voigt symmetry, namely,

$$c_{\alpha\beta\mu\nu} = c_{\beta\alpha\mu\nu} = c_{\alpha\beta\nu\mu} = c_{\mu\nu\alpha\beta}.$$

Indeed, this symmetry is fulfilled by $\underline{\underline{c}}^{\Pi}$ and $\underline{\underline{c}}'$ but not by $\underline{\underline{c}}^{\sigma}$.

The elastic tensors at constant Cauchy stress $\underline{\underline{c}}^{\sigma}$, at constant second Piola–Kirchhoff stress $\underline{\underline{c}}^{\Pi}$ and $\underline{\underline{c}}'$ hence differ by offsets that explicitly depend on the Cauchy stress. The elements of $\underline{\underline{c}}^{\Pi}$ are sometimes called the *Birch coefficients* [4,6,13,33,34]. The elements of $\underline{\underline{c}}'$ govern wave propagation [5,6].

The fact that we cannot write a thermodynamic potential for constant Cauchy stress means that the work on the system depends on the deformation path. This is illustrated in Fig. 2, which compares the work at constant Cauchy stress with a constant second-Piola-Kirchhoff-stress. As should become
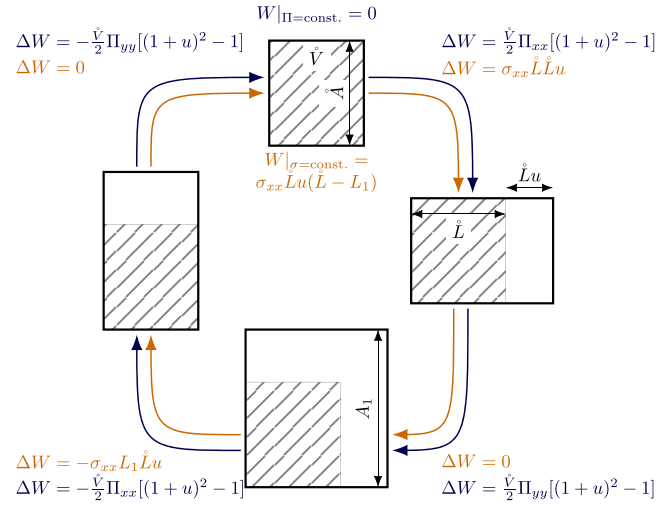
FIG. 2. Mechanical work required to deform an RVE along a simple, exemplary closed deformation path while maintaining either the Cauchy stress $\underline{\sigma}$ or the Piola–Kirchhoff stress $\underline{\Pi}$ constant. At constant $\underline{\sigma}$ (blue), the work around this cycle is not zero while it is zero at constant $\underline{\Pi}$ (orange). The reason for this is that when extending the area $\mathring{A}$ to A_1, the effective force on this area increases at constant $\underline{\sigma}$ but is constant at constant $\underline{\Pi}$. This path dependence implies that the state of the bath has changed after this cycle at constant $\underline{\sigma}$.

clear from this illustration, the reason for this path dependence is that to maintain a constant Cauchy stress, the embedding medium needs to adjust the force on the system to its shape, e.g., by applying a constant stress on the *yz* plane and another constant stress on the *xz* plane. In the context of molecular dynamics simulations, this means that extended system methods for simulations at constant nonisotropic Cauchy stress cannot be formulated [30]. The classical Parinello–Rahman method [27] maintains constant $\underline{\Pi}$ and controlling the *Cauchy* stress requires nonconservative methods [30].

The Birch coefficients fulfill Voigt symmetry under purely hydrostatic pressure P where $\sigma_{\alpha\beta} = -P\delta_{\alpha\beta}$ [4]. This path dependence hence disappears in the classical thermodynamic treatment that only considers changes in volume, as outlined in Sec. II D.

G. Non-affine displacements

The assumption that the deformation of an RVE is purely homogeneous and affine cannot be generally transferred to a (continuum) micromechanical or atomistic description of solids. In most systems, atoms experience forces in the affinely deformed state that drive them into a new equilibrium position [16,17,21,35]. To capture this effect, we modify Eq. (1) and write the new equilibrium positions as

$$\vec{r}_i = \underline{F} \cdot \mathring{\vec{r}}_i + \vec{\chi}_i,$$

where $\vec{\chi}_i$ describes the displacement from the affine position of atom i and is called the *nonaffine displacement*. For crystalline materials, a homogeneized continuum model that includes nonaffine atomic displacements is called a *Cauchy-Born* [[17], Chap. 11.2] model by some authors [35]. For

convenience, we will work below with scaled coordinates $\vec{s}_i$, defined such that

$$\vec{r}_i = \underline{h} \cdot (\overset{\circ}{\vec{s}}_i + \vec{\Psi}_i),$$

with the scaled nonaffine displacements $\vec{\Psi}_i$. This allows us to decouple variation of (scaled) positions and variation of strain.

To understand the effect of nonaffine displacements, we now turn to a variational formulation of the elastic coefficients, as, for example, employed in stochastic micromechanical homogenization [36,37] seeking effective elastic coefficients for an (elastically) heterogeneous medium. The variational formulation requires a thermodynamic potential and we can only carry it out at constant second Piola–Kirchhoff stress $\underline{\Pi}$. We search for the elastic coefficients $\underline{\underline{C}}^{\Pi}$, such that

$$\tfrac{1}{2}\overset{\circ}{V}\eta_{\alpha\beta}C^{\Pi}_{\alpha\beta\mu\nu}\eta_{\mu\nu} = \min_{\{\vec{\Psi}_i\}} g(\{\vec{\Psi}_i\}, \underline{\Pi}; \underline{\eta}) \quad (23)$$

for suitably small $\underline{\eta}$. Without nonaffine displacements ($\vec{\Psi}_i = 0$), this immediately leads to the (affine) elastic coefficients $\underline{\underline{c}}^{\Pi}$ given by Eq. (22).

We expand the extended Gibbs free energy, i.e., the right-hand side of Eq. (23), to second order in both strain and nonaffine displacements around the equilibrium positions $\vec{\Psi}_i = 0$. Note that $\partial g/\partial \vec{\Psi}_i = 0$ at equilibrium, otherwise the atoms would move without perturbation of the RVE. This yields

$$g(\{\vec{\Psi}_i\}, \underline{\Pi}; \underline{\eta}) = \tfrac{1}{2}\overset{\circ}{V}\eta_{\alpha\beta}c^{\Pi}_{\alpha\beta\mu\nu}\eta_{\mu\nu}$$
$$+ \tfrac{1}{2}\mathbf{\Psi} \cdot \mathbb{H} \cdot \mathbf{\Psi} + \mathbf{\Psi} \cdot \mathbf{\Gamma}_{\alpha\beta}\eta_{\alpha\beta}, \quad (24)$$

with Hessian $\mathbb{H} = \partial^2 U/\partial\mathbf{\Psi}\partial\mathbf{\Psi}$ and nonaffine forces $\mathbf{\Gamma}_{\alpha\beta} = \partial^2 U/\partial\mathbf{\Psi}\partial\eta_{\alpha\beta}$. Boldface symbols (e.g., $\mathbf{\Psi}$ or $\mathbf{\Gamma}$) indicate DN vectors that combine the individual D vectors ($\vec{\Psi}_i$, $\vec{\Gamma}_i$) for all atoms and bold open symbols (e.g., $\mathbb{H}$) indicate $DN \times DN$ matrices containing the $D \times D$ matrices ($\underline{H}_{ij}$) as blocks. Minimizing Eq. (24) with respect to $\mathbf{\Psi}$ gives $\mathbf{\Psi} = -\mathbb{H}^{-1} \cdot \mathbf{\Gamma}_{\alpha\beta}\eta_{\alpha\beta}$ and inserting this solution into Eq. (24) yields

$$g(\{\vec{\Psi}_i\}, \underline{\Pi}; \underline{\eta}) = \tfrac{1}{2}\overset{\circ}{V}\eta_{\alpha\beta}c^{\Pi}_{\alpha\beta\mu\nu}\eta_{\mu\nu}$$
$$- \tfrac{1}{2}\eta_{\alpha\beta}\mathbf{\Gamma}_{\alpha\beta} \cdot \mathbb{H}^{-1} \cdot \mathbf{\Gamma}_{\mu\nu}\eta_{\mu\nu}.$$

Comparing this with the left-hand side of Eq. (23), we see that the finite stress elastic coefficients, including the effect of nonaffine displacements, are given by

$$C^{\Pi}_{\alpha\beta\mu\nu} = c^{\Pi}_{\alpha\beta\mu\nu} - \frac{1}{\overset{\circ}{V}}\mathbf{\Gamma}_{\alpha\beta} \cdot \mathbb{H}^{-1} \cdot \mathbf{\Gamma}_{\mu\nu}. \quad (25)$$

Equation (25) is identical to what has been reported in the literature for the unstressed case, e.g., Ref. [[17], Chap. 11.3.5] or Refs. [19,21,22,38]. Equation (25) with $\underline{\underline{C}}^{\Pi}$ replaced by $\underline{\underline{C}}^{\sigma}$ also holds for the Birch coefficients since the Cauchy stress is not affected by nonaffine displacements.

H. Stability criteria

If a solid is subjected to mechanical load, it can become unstable and undergo either a polymorphic phase transition or, for crystals, transform into an amorphous state [39,40].

The RVE remains mechanically stable as long as small perturbations of either atomic positions or h matrix do not lead to a decrease in energy. This is equivalent to stating that all eigenvalues of the total Hessian of the RVE, given by the matrix

$$\mathcal{H} = \begin{pmatrix} \mathbb{H} & \mathbf{\Gamma}^T \\ \mathbf{\Gamma} & \underline{\underline{c}}^{\Pi} \end{pmatrix} \quad (26)$$

of second derivatives of the extended Gibbs free energy $g(\mathbf{\Psi}, \underline{\eta})$, are nonnegative. This is equivalent to stating that the quadratic form

$$\begin{pmatrix} \mathbf{\Psi} \\ \underline{\eta} \end{pmatrix} \cdot \begin{pmatrix} \mathbb{H} & \mathbf{\Gamma}^T \\ \mathbf{\Gamma} & \underline{\underline{c}}^{\Pi} \end{pmatrix} \cdot \begin{pmatrix} \mathbf{\Psi} \\ \underline{\eta} \end{pmatrix} \quad (27)$$

must be nonnegative for small $\mathbf{\Psi}$ and $\underline{\eta}$. We can write a related quadratic form in terms of the forces $\mathbf{\bar{f}}$ and stresses $\underline{\sigma}$,

$$\begin{pmatrix} \mathbf{f} \\ \underline{\sigma} \end{pmatrix} \cdot \begin{pmatrix} \mathbb{H} & \mathbf{\Gamma}^T \\ \mathbf{\Gamma} & \underline{\underline{c}}^{\Pi} \end{pmatrix}^{-1} \cdot \begin{pmatrix} \mathbf{f} \\ \underline{\sigma} \end{pmatrix}, \quad (28)$$

which also must be nonnegative for small $\mathbf{f}$ and $\underline{\sigma}$. Equation 28 has to be interpreted as the pseudoinverse, as the overall Hessian is not formally invertible because of translational invariance of the system.

The variety of stability criteria found in the literature are most easily described using Eqs. (27) and (28). Assuming a fixed cell ($\eta = 0$), the system remains stable as long as all normal mode frequencies (given by the eigenvalues of $\mathbb{H}$) are positive. This is known as the *dynamical* [8,41,42] or *phonon stability* [35]. Under fixed positions ($\mathbf{\Psi} = 0$), the system remains stable as long as the eigenvalues of $\underline{\underline{c}}^{\Pi}$ are positive. This is known as the *Born* [8,9,11,13,14,41,43] or *homogeneized-continuum stability criterion* [35]. If we assume that the forces on all atoms vanish ($\mathbf{f} = 0$), the eigenvalues of the bottom right block of $\mathcal{H}^{-1}$ must vanish. It is straightforward to show that this block is given by Eq. (25), the elastic coefficients tensor $\underline{\underline{C}}^{\Pi}$ that includes the effect of nonaffine displacements. If nonaffine displacements are explicitly considered, the instability is sometimes referred to as a *Cauchy-Born instability* [35]. Violation of Born or Cauchy-Born stability is called an *elastic instability* [11,13,14,42,43].

There are a few subtleties to consider. First, the limit of stability (either mechanic or dynamic) depends on the symmetry of the crystal, the deformation mode and the crystal orientation or the direction of deformation. Therefore, the critical stress for an instability is best represented by a surface in three-dimensional space. Second, dynamical or elastic stability are only necessary, not sufficient conditions for stability. This is because stability is governed by $\mathcal{H}$, while regarding either dynamical or elastic stability considers only one of the diagonal blocks $\mathbb{H}$ and $\underline{\underline{c}}^{\Pi}$. Those couple through $\underline{\underline{\mathbf{\Gamma}}}$, and this coupling will generally decrease the lowest individual eigenvalue. Third, stability depends on the strain measure that is used to describe cell deformation. For example, using the small strain tensor $\underline{\varepsilon}$ in lieu of the Lagrange strain $\underline{\eta}$ for constructing the global Hessian $\mathcal{H}$ will lead to the occurrence of the elastic coefficients tensor $\underline{\underline{c}}'$ [defined in Eq. (19)] as the bottom right block of Eq. (26). The stability of a molecular calculation run with a Parinello-Rahman barostat, for example, requires $\underline{\underline{C}}^{\Pi}$ to be positive definite. In general, stability

therefore depends on the type of elastic embedding medium used for the RVE and the boundary conditions on the boundary of this medium. For example, stability of a solid near a crack tip will be different from stability in a bending beam.

Fourth, stability at constant Cauchy stress needs to be discussed separately. It does not emerge from a systematic expansion of *g*, and as a consequence $\underline{\underline{C}}^\sigma$ is not symmetric for multiaxial stress. Elastic stability implies that the quadratic form

$$\eta_{\alpha\beta} C^\sigma_{\alpha\beta\mu\nu} \eta_{\mu\nu}$$

remains positive for nonzero η. We can decompose the tensor $C^\sigma_{\alpha\beta\mu\nu}$ into its symmetric $C^{\text{sym}}_{\alpha\beta\mu\nu}$ and antisymmetric part $C^{\text{asym}}_{\alpha\beta\mu\nu}$, where $C^{\text{sym}}_{\alpha\beta\mu\nu} = (C^\sigma_{\alpha\beta\mu\nu} + C^\sigma_{\mu\nu\alpha\beta})/2$ and $C^{\text{asym}}_{\alpha\beta\mu\nu} = (C^\sigma_{\alpha\beta\mu\nu} - C^\sigma_{\mu\nu\alpha\beta})/2$. This yields

$$\eta_{\alpha\beta} C^{\text{sym}}_{\alpha\beta\mu\nu} \eta_{\mu\nu} + \eta_{\alpha\beta} C^{\text{asym}}_{\alpha\beta\mu\nu} \eta_{\mu\nu}.$$

It is easy to see that the second expression is always zero, since $C^{\text{asym}}_{\alpha\beta\mu\nu} = -C^{\text{asym}}_{\mu\nu\alpha\beta}$. The stability condition then requires $C^{\text{sym}}_{\alpha\beta\mu\nu}$ to be positive definite. For crystals, it is possible to derive closed-form expressions for this condition. A summary of necessary and sufficient conditions for common crystal structures is given in Ref. [42].

Fifth, for solids in which the nonaffine contribution to the elastic coefficients is not negligible, the dynamical and the elastic stability criteria are not independent of each other. To see this, we perform a diagonalization of the Hessian $\mathbb{H} = \mathbb{S}\mathbb{D}\mathbb{S}^{-1}$. Here, $\mathbb{S} = (\mathbf{e}_1, \ldots, \mathbf{e}_{3N})$ is a square matrix whose *p*th column is the eigenvector $\mathbf{e}_p$ of $\mathbb{H}$ and $\mathbb{D}$ is a diagonal matrix whose elements are the eigenvalues λ_p. The Hessian evaluated at a local minimum is positive semidefinite, in particular, $\lambda_p > 0$ (for $p > D$) while the first *D* eigenvalues are zero. We can now express the inverse Hessian $\mathbb{H}^{-1}$ in Eq. (25) through its eigenvectors and eigenvalues,

$$-\frac{1}{\mathring{V}} \boldsymbol{\Gamma}_{\alpha\beta} \cdot \mathbb{H}^{-1} \cdot \boldsymbol{\Gamma}_{\mu\nu} = -\frac{1}{\mathring{V}} \sum_p \frac{\hat{\Gamma}_{p,\alpha\beta} \hat{\Gamma}_{p,\mu\nu}}{\lambda_p},$$

where we have implicitly excluded the translational degrees of freedom from the sum. The quantity $\hat{\Gamma}_{p,\alpha\beta} = \boldsymbol{\Gamma}_{\alpha\beta} \cdot \mathbf{e}_p$ is the projection of the nonaffine forces on the eigenvectors of the Hessian. If one eigenvalue λ is small (but finite), the nonaffine contribution of this mode will be a large negative value, which may lead to at least one very small elastic tensor element, unless the projected nonaffine forces disappear. In crystals, most of the $\hat{\Gamma}_{p,\alpha\beta}$ are zero because of symmetry. Nonzero $\hat{\Gamma}_{p,\alpha\beta}$ only occur for crystals which have more than one nonequivalent Wyckoff position. This means in crystals, elastic instabilities are largely decoupled from dynamical instabilities. Conversely, in amorphous materials $\hat{\Gamma}_{p,\alpha\beta}$ are generally nonzero and the instabilities are closely coupled.

Nevertheless, this relation does not necessarily imply that a dynamically unstable solid is also elastically unstable. Consider, for example, a solid filled with gas molecules which can move freely, such as a zeolite filled with air [44]. In this case, the Hessian matrix $\mathbb{H}$ is certainly not positive definite, which implies that the system is not dynamically stable (because the air molecules can move), yet the solid remains elastically stable. In the context of random networks, stability is explained by the concept of rigidity percolation, and rigid networks can contain floppy regions without losing overall stability [45–48].

III. MANY-BODY INTERATOMIC POTENTIALS

A. Specific functional forms

To compute the elastic coefficients using analytical expressions, we need the second-order derivatives of the potential energy with respect to strain and atomic positions. This yields the Born elastic coefficients $\underline{\underline{c}}^\Pi$, the nonaffine forces $\boldsymbol{\Gamma}_{\alpha\beta}$, and the Hessian $\mathbb{H}$ of the underlying potential. We here outline these expressions for many-body interatomic potentials [17,25,49] at zero temperature. Noise induced by thermal [17,50] but also quantum-mechanical [51] fluctuations yields additional contributions to the stiffness coefficients. They must be added to those derived here for systems at finite temperature.

While specific expressions for cluster potentials and embedded atom method potentials can be found in the literature, for example, in Ref. [[17], Chap. 11.5.2], we here present a more general treatment, which applies for complex cluster functionals (such as Tersoff-Brenner potentials [52–54]) through the generic functional form of [25]

$$U = \frac{1}{2} \sum_{\substack{ij \\ i \neq j}} \left[U_2(r_{ij}^2) + U_{\text{m}}(r_{ij}^2, \xi_{ij}) \right], \tag{29}$$

with

$$\xi_{ij} = \sum_{\substack{k \\ k \neq i,j}} \Xi(r_{ij}^2, r_{ik}^2, r_{jk}^2). \tag{30}$$

Here $r_{ij} = |\vec{r}_{ij}|$ is the distance between atoms *i* and *j*. The three-body term, Eq. (30), describes the triplet through the three side lengths of the triangle that it forms. We express everything in terms of the squares of the distances, which simplifies derivatives with respect to the Green–Lagrange strain. This mathematical trick has first been used by Born [8,9].

Our formulation trivially includes pair potentials $V(r_{ij})$:

$$U_2(r_{ij}^2) = V(r_{ij}) \quad \text{and} \quad U_{\text{m}} = 0.$$

Furthermore, we can represent potentials of the Abell–Tersoff–Brenner [52–54] type. For example, the multicomponent Tersoff potential [55] is given by

$$U_2(r_{ij}^2) = f_{\text{C}}(r_{ij}) A_{ij} \exp(-\lambda_{ij} r_{ij}),$$

$$U_{\text{m}}(r_{ij}^2, \xi_{ij}) = -f_{\text{C}}(r_{ij}) b_{ij}(\xi_{ij}) B_{ij} \exp(-\mu_{ij} r_{ij}),$$

and

$$\Xi(r_{ij}^2, r_{ik}^2, r_{jk}^2) = f_{\text{C}}(r_{ik}) \left[1 + \frac{c_i^2}{d_i^2} - \frac{c_i^2}{d_i^2 + (h_i - \cos\theta_{ijk})^2} \right],$$

with

$$b_{ij}(\xi_{ij}) = \chi_{ij}(1 + (\beta_i \xi_{ij})^{n_i})^{-1/2n_i}$$

$$f_{\text{C}}(r) = \begin{cases} 1, & r \leqslant r_1 \\ \frac{1}{2}\left(1 + \cos\left(\pi \frac{r - r_1}{r_2 - r_1}\right)\right), & r_1 < r < r_2 \\ 0, & r_2 \leqslant r, \end{cases}$$

where $\cos\theta_{ijk} = (r_{ij}^2 + r_{ik}^2 - r_{jk}^2)/(2r_{ij}r_{ik})$ and f_C is a cutoff function that varies smoothly from unity to zero between two distances. The quantities A_{ij}, B_{ij}, λ_{ij}, μ_{ij}, χ_{ij}, β_i, n_i, c_i, d_i, h_i, r_1, and r_2 are parameters (see Ref. [55] for more information).

This generic functional form is also suitable for cluster potentials which include interactions only up to three-body terms. One frequently used example of this class of potentials is the Stillinger–Weber potential, whose expressions in our formulation read [56]

$$U_2(r_{ij}^2) = f_{C1}(r_{ij})A\epsilon\left[B\left(\frac{\sigma}{r_{ij}}\right)^p - \left(\frac{\sigma}{r_{ij}}\right)^q\right]$$

$$U_m(r_{ij}^2, \xi_{ij}) = \epsilon\lambda\xi_{ij}$$

and

$$\Xi(r_{ij}^2, r_{ik}^2, r_{jk}^2) = f_{C2}(r_{ik})f_{C2}(r_{ij})[\cos(\theta_{ijk}) - \cos(\theta_0)]^2,$$

with

$$f_{C1}(r) = H(a\sigma - r)\exp\left(\frac{\sigma}{r - a\sigma}\right),$$

$$f_{C2}(r) = H(a\sigma - r)\exp\left(\frac{\gamma\sigma}{r - a\sigma}\right),$$

where H is the Heaviside step function, $\cos(\theta_0) = -1/3$ is the tetrahedral angle, while σ, ϵ, A, B, p, q, a, λ, and γ are parameters. The values for the original parametrization can be found in Ref. [56].

B. Generic form of the first derivatives

In the following, we use the shorthand notation $R_{ij} = r_{ij}^2$ so the square is not mistaken as a second-order derivative. Three derivatives will appear repeatedly in the following. First, we need the derivative of R_X with respect to the atomic positions

$$\frac{\partial R_X}{\partial r_{n,\beta}} = 2\pi_{X|n}r_{X,\beta} \quad\text{and}\quad \frac{\partial^2 R_X}{\partial r_{m,\alpha}\partial r_{n,\beta}} = 2\pi_{X|n}\pi_{X|m}\delta_{\alpha\beta},$$

with $X \in \{ij, ik, jk\}$ and $\pi_{ij|n} = \delta_{in} - \delta_{jn}$. Second, we need the derivative of R_X with respect to the Green–Lagrange strain tensor $\underline{\eta}$. Using $R_X = \mathring{r}_{X,\alpha}(\delta_{\alpha\beta} + 2\eta_{\alpha\beta})\mathring{r}_{X,\beta}$, we obtain

$$\frac{\partial R_X}{\partial \eta_{\alpha\beta}} = 2\mathring{r}_{X,\alpha}\mathring{r}_{X,\beta} \quad\text{and}\quad \frac{\partial^2 R_X}{\partial \eta_{\alpha\beta}\partial \eta_{\mu\nu}} = 0.$$

Finally, we consider the mixed derivative with respect to the atomic positions and the Green–Lagrange strain, which reads

$$\frac{\partial^2 R_X}{\partial \mathring{r}_{n,\gamma}\partial \eta_{\alpha\beta}} = 2\pi_{X|n}(\mathring{r}_{X,\beta}\delta_{\gamma\alpha} + \mathring{r}_{X,\alpha}\delta_{\gamma\beta}).$$

Using these derivatives, we can directly write down the expression for the forces

$$\vec{f}_n \equiv -\frac{\partial U}{\partial \vec{r}_n} = -\sum_{\substack{ij\\i\neq j}}\left(\pi_{ij|n}\left[\frac{\partial U_2}{\partial R_{ij}} + \frac{\partial U_m}{\partial R_{ij}}\right]\vec{r}_{ij}\right.$$

$$\left. + \sum_{\substack{k\\k\neq i,j}}\sum_X \pi_{X|n}\frac{\partial U_m}{\partial \xi_{ij}}\frac{\partial \Xi}{\partial R_X}\vec{r}_X\right)$$

and the stress tensor

$$\sigma_{\alpha\beta}^{U\eta} \equiv \frac{1}{\mathring{V}}\frac{\partial U}{\partial \eta_{\alpha\beta}} = \frac{1}{\mathring{V}}\sum_{\substack{ij\\i\neq j}}\left(\left[\frac{\partial U_2}{\partial R_{ij}} + \frac{\partial U_m}{\partial R_{ij}}\right]r_{ij,\alpha}r_{ij,\beta}\right.$$

$$\left. + \sum_{\substack{k\\k\neq i,j}}\sum_X \frac{\partial U_m}{\partial \xi_{ij}}\frac{\partial \Xi}{\partial R_X}r_{X,\alpha}r_{X,\beta}\right).$$

C. Generic form of the second derivatives

We need general second-order derivatives of the form $\partial^2 U/\partial a\partial b$, where a and b can be components of the Green-Lagrange strain $\underline{\eta}$ (yielding the Born elastic coefficients), components of the position vector $\vec{r}$ (yielding the Hessian), or combinations of both (yielding the nonaffine forces). We now write these for the generic form of the many-body potential given by Eqs. (29) and (30). The potential-specific derivatives of the functions U_2, U_m, and Ξ appearing in the various expressions are left as exercises to the reader; they can also be found in our implementation included in the software package MATSCIPY [26]. Taking the second derivative of Eq. (29) yields

$$\frac{\partial^2 U}{\partial a\partial b} = \frac{1}{2}\sum_{\substack{ij\\i\neq j}}\left\{\underbrace{\left[\frac{\partial U_2}{\partial R_{ij}} + \frac{\partial U_m}{\partial R_{ij}}\right]\frac{\partial^2 R_{ij}}{\partial a\partial b}}_{\text{term 1}}\right.$$

$$+ \underbrace{\left[\frac{\partial^2 U_2}{\partial R_{ij}^2} + \frac{\partial^2 U_m}{\partial R_{ij}^2}\right]\frac{\partial R_{ij}}{\partial a}\frac{\partial R_{ij}}{\partial b}}_{\text{term 2}} + \underbrace{\frac{\partial U_m}{\partial \xi_{ij}}\frac{\partial^2 \xi_{ij}}{\partial a\partial b}}_{\text{term 3}}$$

$$+ \underbrace{\frac{\partial^2 U_m}{\partial R_{ij}\partial \xi_{ij}}\left(\frac{\partial R_{ij}}{\partial a}\frac{\partial \xi_{ij}}{\partial b} + \frac{\partial \xi_{ij}}{\partial a}\frac{\partial R_{ij}}{\partial b}\right)}_{\text{term 4}}$$

$$+ \underbrace{\frac{\partial^2 U_m}{\partial \xi_{ij}^2}\frac{\partial \xi_{ij}}{\partial a}\frac{\partial \xi_{ij}}{\partial b}}_{\text{term 5}}\left.\right\}. \tag{31}$$

Furthermore, the first derivative of ξ_{ij} can be expressed as

$$\frac{\partial \xi_{ij}}{\partial a} = \sum_{\substack{k\\k\neq i,j}}\sum_X \frac{\partial \Xi(R_{ij}, R_{ik}, R_{jk})}{\partial R_X}\frac{\partial R_X}{\partial a}$$

and its second derivative is given by

$$\frac{\partial^2 \xi_{ij}}{\partial a\partial b} = \sum_{\substack{k\\k\neq i,j}}\sum_{XY}\frac{\partial R_X}{\partial a}\frac{\partial^2 \Xi(R_{ij}, R_{ik}, R_{jk})}{\partial R_X\partial R_Y}\frac{\partial R_Y}{\partial b}$$

$$+ \sum_{\substack{k\\k\neq i,j}}\sum_X \frac{\partial \Xi(R_{ij}, R_{ik}, R_{jk})}{\partial R_X}\frac{\partial^2 R_X}{\partial b\partial a}, \tag{32}$$

with $X, Y \in \{ij, ik, jk\}$. In the following subsections, we provide analytic expressions for the Born elastic coefficients, the nonaffine forces, and the Hessian. Each of these expressions along with the interatomic potentials from Sec. III A were tested for correctness against finite differences.

D. Born elastic coefficients

For the calculation of the (Born) elastic coefficients, we need to evaluate $\mathring{V} c^{\Pi\eta}_{\alpha\beta\mu\nu} = \partial^2 U / \partial \eta_{\alpha\beta} \partial \eta_{\mu\nu}$, hence both a and b are components of the Green-Lagrange strain tensor $\underline{\eta}$. It is then straightforward to evaluate the individual terms for the Born elastic coefficients,

$$\mathring{V} c^{\Pi\eta(1)}_{\alpha\beta\mu\nu} = 0,$$

$$\mathring{V} c^{\Pi\eta(2)}_{\alpha\beta\mu\nu} = 2 \sum_{\substack{ij \\ i \neq j}} \left[\frac{\partial^2 U_2}{\partial R^2_{ij}} + \frac{\partial^2 U_{\mathrm{m}}}{\partial R^2_{ij}} \right] \mathring{r}_{ij,\alpha} \mathring{r}_{ij,\beta} \mathring{r}_{ij,\mu} \mathring{r}_{ij,\nu},$$

$$\mathring{V} c^{\Pi\eta(3)}_{\alpha\beta\mu\nu} = 2 \sum_{\substack{ij \\ i \neq j}} \sum_{\substack{k \\ k \neq i,j}} \sum_{XY} \frac{\partial U_{\mathrm{m}}}{\partial \xi_{ij}} \frac{\partial^2 \Xi}{\partial R_X \partial R_Y} \mathring{r}_{X,\alpha} \mathring{r}_{X,\beta} \mathring{r}_{Y,\mu} \mathring{r}_{Y,\nu},$$

$$\mathring{V} c^{\Pi\eta(4)}_{\alpha\beta\mu\nu} = 2 \sum_{\substack{ij \\ i \neq j}} \sum_{\substack{k \\ k \neq i,j}} \sum_X \frac{\partial^2 U_{\mathrm{m}}}{\partial R_{ij} \partial \xi_{ij}} \frac{\partial \Xi}{\partial R_X} (\mathring{r}_{ij,\alpha} \mathring{r}_{ij,\beta} \mathring{r}_{X,\mu} \mathring{r}_{X,\nu} + \mathring{r}_{X,\alpha} \mathring{r}_{X,\beta} \mathring{r}_{ij,\mu} \mathring{r}_{ij,\nu}),$$

$$\mathring{V} c^{\Pi\eta(5)}_{\alpha\beta\mu\nu} = 2 \sum_{\substack{ij \\ i \neq j}} \frac{\partial^2 U_{\mathrm{m}}}{\partial \xi^2_{ij}} \left(\sum_{\substack{k \\ k \neq i,j}} \sum_X \frac{\partial \Xi}{\partial R_X} \mathring{r}_{X,\alpha} \mathring{r}_{X,\beta} \right) \left(\sum_{\substack{l \\ l \neq i,j}} \sum_Y \frac{\partial \Xi}{\partial R_Y} \mathring{r}_{Y,\mu} \mathring{r}_{Y,\nu} \right),$$

with $X \in \{ij, ik, jk\}$ and with $Y \in \{ij, il, jl\}$.

E. Non-affine forces

For the nonaffine forces, b becomes a component of a reference atomic position $\mathring{r}_{n,\gamma}$ and a needs to be replaced with a component of the strain tensor $\eta_{\alpha\beta}$. The five individual terms of Eq. (31) yield

$$\Gamma^{(1)}_{n\gamma,\alpha\beta} = \sum_{\substack{ij \\ i \neq j}} \pi_{ij|n} \left[\frac{\partial U_2}{\partial R_{ij}} + \frac{\partial U_{\mathrm{m}}}{\partial R_{ij}} \right] (\mathring{r}_{ij,\beta} \delta_{\alpha\gamma} + \mathring{r}_{ij,\alpha} \delta_{\beta\gamma}),$$

$$\Gamma^{(2)}_{n\gamma,\alpha\beta} = 2 \sum_{\substack{ij \\ i \neq j}} \pi_{ij|n} \left[\frac{\partial^2 U_2}{\partial R^2_{ij}} + \frac{\partial^2 U_{\mathrm{m}}}{\partial R^2_{ij}} \right] \mathring{r}_{ij,\alpha} \mathring{r}_{ij,\beta} \mathring{r}_{ij,\gamma},$$

$$\Gamma^{(3)}_{n\gamma,\alpha\beta} = 2 \sum_{\substack{ij \\ i \neq j}} \sum_{\substack{k \\ k \neq ij}} \sum_{XY} \pi_{Y|n} \frac{\partial U_{\mathrm{m}}}{\partial \xi_{ij}} \frac{\partial^2 \Xi}{\partial R_X \partial R_Y} \mathring{r}_{X,\alpha} \mathring{r}_{X,\beta} \mathring{r}_{Y,\gamma}$$

$$+ \sum_{\substack{ij \\ i \neq j}} \sum_{\substack{k \\ k \neq ij}} \sum_X \frac{\partial U_{\mathrm{m}}}{\partial \xi_{ij}} \frac{\partial \Xi}{\partial R_X} \pi_{X|n} (\mathring{r}_{X,\beta} \delta_{\alpha\gamma} + \mathring{r}_{X,\alpha} \delta_{\beta\gamma}),$$

$$\Gamma^{(4)}_{n\gamma,\alpha\beta} = 2 \sum_{\substack{ij \\ i \neq j}} \sum_{\substack{k \\ k \neq ij}} \sum_X \frac{\partial^2 U_{\mathrm{m}}}{\partial R_{ij} \partial \xi_{ij}} \frac{\partial \Xi}{\partial R_X} (\pi_{ij|n} \mathring{r}_{X,\alpha} \mathring{r}_{X,\beta} \mathring{r}_{ij,\gamma} + \pi_{X|n} \mathring{r}_{ij,\alpha} \mathring{r}_{ij,\beta} \mathring{r}_{X,\gamma}),$$

$$\Gamma^{(5)}_{n\gamma,\alpha\beta} = 2 \sum_{\substack{ij \\ i \neq j}} \frac{\partial^2 U_{\mathrm{m}}}{\partial \xi^2_{ij}} \left(\sum_{\substack{k \\ k \neq ij}} \sum_X \frac{\partial \Xi}{\partial R_X} \mathring{r}_{X,\alpha} \mathring{r}_{X,\beta} \right) \left(\sum_{\substack{l \\ l \neq ij}} \sum_Y \pi_{Y|n} \frac{\partial \Xi}{\partial R_Y} \mathring{r}_{Y,\gamma} \right),$$

with $X \in \{ij, ik, jk\}$ and $Y \in \{ij, il, jl\}$.

F. Hessian

Starting again from Eq. (31) and replacing a as well as b with components of current atomic positions $r_{m,\alpha}$ and $r_{n,\beta}$ yields the individual expressions for the off-diagonal components of the Hessian. Note that the expressions given here differ from the components of $\mathbb{H}$, which are the derivatives with respect to scaled positions. The (second) derivatives with respect to actual

positions are given by

$$H_{m\alpha,n\beta}^{(1)} = \sum_{\substack{ij \\ i \neq j}} \tau_{ij,ij|mn}\left[\frac{\partial U_2}{\partial R_{ij}} + \frac{\partial U_{\mathrm{m}}}{\partial R_{ij}}\right]\delta_{\alpha\beta},$$

$$H_{m\alpha,n\beta}^{(2)} = 2\sum_{\substack{ij \\ i \neq j}} \tau_{ij,ij|mn}\left[\frac{\partial^2 U_2}{\partial R_{ij}^2} + \frac{\partial^2 U_{\mathrm{m}}}{\partial R_{ij}^2}\right]r_{ij,\alpha}r_{ij,\beta},$$

$$H_{m\alpha,n\beta}^{(3)} = 2\sum_{\substack{ij \\ i \neq j}}\sum_{\substack{k \\ k \neq ij}}\sum_{XY} \tau_{X,Y|mn}\frac{\partial U_{\mathrm{m}}}{\partial \xi_{ij}}\frac{\partial^2 \Xi}{\partial R_X \partial R_Y}r_{X,\alpha}r_{Y,\beta}$$

$$+ \sum_{\substack{ij \\ i \neq j}}\sum_{\substack{k \\ k \neq ij}}\sum_{X} \tau_{X,X|mn}\frac{\partial U_{\mathrm{m}}}{\partial \xi_{ij}}\frac{\partial \Xi}{\partial R_X}\delta_{\alpha\beta},$$

$$H_{m\alpha,n\beta}^{(4)} = 2\sum_{\substack{ij \\ i \neq j}}\sum_{\substack{k \\ k \neq ij}}\sum_{X} \frac{\partial^2 U_{\mathrm{m}}}{\partial R_{ij}\partial \xi_{ij}}\frac{\partial \Xi}{\partial R_X}(\tau_{X,ij|mn}r_{X,\alpha}r_{ij,\beta} + \tau_{ij,X|mn}r_{ij,\alpha}r_{X,\beta}),$$

$$H_{m\alpha,n\beta}^{(5)} = 2\sum_{\substack{ij \\ i \neq j}} \frac{\partial^2 U_{\mathrm{m}}}{\partial \xi_{ij}^2}\left(\sum_{\substack{k \\ k \neq ij}}\sum_{X} \pi_{X|m}\frac{\partial \Xi}{\partial R_X}r_{X,\alpha}\right)\left(\sum_{\substack{l \\ l \neq ij}}\sum_{Y} \pi_{Y|n}\frac{\partial \Xi}{\partial R_Y}r_{Y,\beta}\right),$$

with $X \in \{ij, ik, jk\}$ and $Y \in \{ij, il, jl\}$. Furthermore, we have introduced the shorthand notation $\tau_{X,Y|mn} = \pi_{X|m}\pi_{Y|n}$. We know that, by virtue of the symmetry of second derivatives, the full Hessian must be symmetric:

$$H_{m\alpha,n\beta} = H_{n\beta,m\alpha}.$$

We can relate the diagonal and off-diagonal elements of the Hessian with translational invariance. For any translation vector d_α, we have, defining the uniform vector $a_m \equiv 1$,

$$0 = \frac{\partial}{\partial d_\gamma}U(\{a_m d_\alpha\}) = \frac{\partial}{\partial d_\gamma}\left[U(0) + f_{m,\alpha}a_m d_\alpha + \frac{1}{2}a_m d_\alpha H_{m\alpha,n\beta}a_n d_\beta\right] = f_{m,\gamma}a_m + a_m H_{m\gamma,n\beta}a_n d_\beta = a_m H_{m\gamma,n\beta}a_n d_\beta,$$

where we have assumed that conservation of linear momentum $\sum_m f_{m,\gamma} = 0$ holds. The remaining condition is that a_m is an eigenvector associated with a null eigenvalue of the Hessian, which translates to

$$H_{m\alpha,m\beta} = -\sum_{n \neq m}H_{m\alpha,n\beta}.$$

IV. METHODS

To compute elastic properties and analyze lattice stability, it is necessary to first define materials, their specific potential parametrization, initial conditions, employed boundary conditions, and further computational methodology. We have chosen diamond cubic silicon, 3C silicon carbide, and the α-quartz form of silicon dioxide because they are ubiquitous in nature and have tremendous importance for technical applications in electronics, photonics, and photovoltaics [57–60]. In the case of silicon, we consider bond-order potentials as well as one cluster potential [25]. We denote Tersoff's potential [55] as TIII, the refitted version for pure silicon of Erhart and Albe [61] as EAII, the cluster potential by Stillinger and Weber [56] as SW, and the modified Tersoff potential from Kumagai et al. [62] as KUM. The KUM potential differs from the TIII potential by the angular-dependent term and a modified cutoff function. We use the parametrization referred to as MOD in the publication of Kumagai et al. [62]. Similarly,

for silicon carbide, we denote the original parametrization of Tersoff [55] as TIII and its refitted version by Erhart and Albe [61] as EA. For silicon dioxide, we employ the potential by van Beest et al. [63], which we refer to as BKS. The short-range interaction is truncated and shifted at a cutoff distance of $r_c = 10$ Å. Electrostatic interactions are treated using traditional Ewald summation [64,65].

The initial crystalline configurations are set up using the equilibrium lattice constant at zero temperature and pressure for the specific interatomic potential. The simulation cells contain $N \approx 1000$ atoms with periodic boundary conditions in all spatial directions. We first consider the case of hydrostatic pressure $\sigma_{\alpha\beta}^{\eta} = -P\delta_{\alpha\beta}$ in the limit of zero temperature. We follow the convention that a compressing force creates a positive pressure $P > 0$ and causes a negative stress $\sigma < 0$. Hydrostatic loading of the RVE is imposed by first applying an affine transformation $\underline{F} = (1 + \varepsilon)\underline{1}$ with a prescribed strain increment $\varepsilon = 10^{-3}$ to the simulation cell and the atoms and afterwards performing an energy minimization.
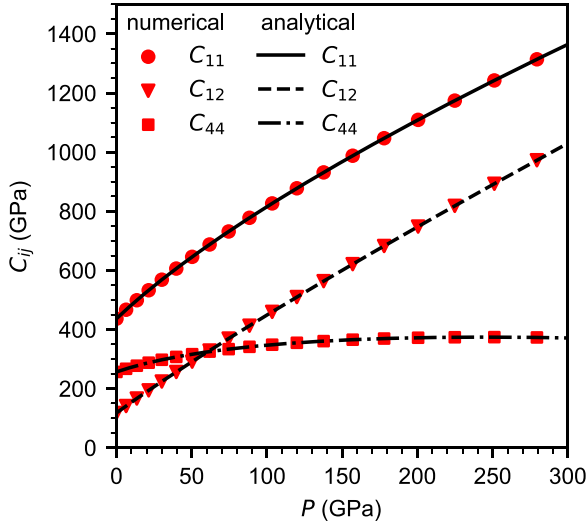
FIG. 3. Numerical and analytical calculations of the elastic coefficients of silicon carbide as a function of pressure. Results are shown for the TIII interatomic potential with a fixed bonding topology.

We note that large hydrostatic compression or tension can lead to nonphysical behavior for interatomic potentials with a finite interaction range. The finite interaction range is typically implemented through a cutoff function making the potential energy and possibly its derivatives vanish at a distance r_c. The reason for this finite interaction is that many potentials are constructed on the assumption of only nearest-neighbor interactions, while further interactions are screened [25,66–69]. The value of r_c is then typically chosen to lie between first and second neighbor shell in the ground-state crystal. Volumetric deformation, however, does not change nearest neighbor relationships, yet using a fixed finite interaction range will lead to unphysical zero-energy configurations at large volumetric strain. For crystalline structures that do not change their bonding topology, a simple remedy is to retain nearest-neighbor interactions up to arbitrary distances, effectively replacing the cutoff-procedure by a fixed bond topology [20,70]. In the following, we denote potentials where the bond topology is determined for the ideal crystal and kept fixed during deformation by appending +FT to the potential names defined in the last paragraph, e.g., for Tersoff's potential TIII + FT.

For all employed interatomic potentials, we checked consistency of the analytical expressions from Sec. III with numerical results obtained from finite difference computations. In Fig. 3, we show exemplarily a comparison between numerical and analytical results for one interatomic potential for silicon carbide. Due to the small strain increment and the resulting large number of elastic coefficients, we replace the discrete values of the analytic results by a line. From this figure, it is evident that if proper parameters are chosen for the finite difference computation, both approaches to compute elastic coefficients lead to similar results.

V. RESULTS

A. Elastic coefficients at zero stress

We first compute the elastic coefficients at zero hydrostatic pressure. This serves as a validation for the analytical

expressions and enables us to determine, which interatomic potential best describes the elastic properties of the material under investigation. The different elastic coefficients are only equivalent in the limiting case of zero external stress [4]. We restrict our discussion to the Birch coefficients and will omit in the following the superscripts of the elastic coefficients even at nonzero external stress, $C_{\alpha\beta\mu\nu} \equiv C^{\sigma}_{\alpha\beta\mu\nu}$. Table I shows a comparison of the equilibrium lattice constants and the elastic coefficients. We compare experimental results, density functional theory (DFT) calculations, results from reference publications, and our values from analytical calculations. When reporting values, we condense the four indices of the elastic coefficients tensors to two using Voigt (or Nye) notation [71,72]. Silicon and silicon carbide have a cubic lattice symmetry with three independent elastic coefficients C_{11}, C_{12}, and C_{44}. In contrast, α-quartz has a trigonal crystal structure with six independent elastic moduli C_{11}, C_{12}, C_{13}, C_{14}, C_{33}, and C_{44}.

For silicon, the relative error of the lattice constant and the elastic coefficients between our results and the reference publications is smaller than 0.01% for the KUM and the TIII potential. For the SW potential, we observe small relative errors in the order of 0.1% for the elastic coefficients, which include nonaffine displacements, and a large relative error of 7.32% for c_{44}, which does not take nonaffine displacements into account. This larger error for c_{44} is probably related to the parameters of the finite difference approach in the Ref. [75]. For the EAII potential, we observe small relative errors of up to 2.4% in the elastic coefficients with respect to the reference values [61]. This is likely due to the discrepancy in the lattice constant compared to the original publication. We repeated our computation using the reference lattice constant of $a = 5.429$ Å and obtained $C_{11} = 169.24$ GPa, $C_{12} = 64.16$ GPa, $C_{44} = 71.67$ GPa and $c_{44} = 110.99$ GPa. Using the reference lattice constant decreases the maximal relative error of the elastic coefficients between our results and the reference values to 1.34%. Based on our results, the relative error between the elastic coefficients from experiments and DFT is smallest for the KUM potential.

For silicon carbide, we observe a maximal relative error between the reference values and our results of 0.46% for the EA potential and 3.8% for the TIII potential. The largest error relative to experiments is 6.8% and 20.4%, while the error relative to the DFT values is at most 8.4% and 22.9% for the EA and the TIII, respectively. Although EA and TIII are based on the same functional form, the EA parametrization improves the accuracy of the lattice constant and the elastic coefficients with respect to the experimental and the DFT results significantly.

For α-quartz, the errors between our results and the original publication are less than 1.0%. Despite the comparatively simple functional form of the BKS potential, the relative errors of the structural and elastic properties with respect to the reference data from experiments and DFT-LDA data are below 28% and 56%, respectively. For the DFT-GGA data, the maximal relative error is about 200% which appears for the C_{12} value. Comparing experiments to the *ab initio* computations, it is evident that the DFT-LDA results are in better agreement with the experimental values [78]. We further note that more complex potentials do not provide a significant

TABLE I. Zero-stress lattice constants and elastic coefficients for silicon, silicon carbide, and silicon dioxide. a_0, c_0: Lattice constants. C_{ij}: Elastic coefficients with nonaffine contribution. c_{ij}: Elastic coefficients without nonaffine contribution.

	Silicon						
	Expt.	DFT-LDA		TIII		EA Si-II	
	Ref.[b]	Ref.[k]	Ref.[c]	Ref.[e]	This paper	Ref.[a]	This paper
a_0 (Å)	5.431	5.400	5.406	5.432	5.432	5.429	5.432
C_{11} (GPa)	166	159	160	142.5	142.54	167	168.48
C_{12} (GPa)	64	61	63	75.4	75.38	65	63.47
C_{44} (GPa)	80	85	82	69	69.03	72	71.53
c_{44} (GPa)		111	112	118.8	118.81	111	110.44

	KUM		SW				
	Ref.[f]	This paper	Ref.[l]	This paper			
a_0 (Å)	5.429	5.429	5.431	5.431			
C_{11} (GPa)	166.4	166.37	151.4	151.42			
C_{12} (GPa)	65.3	65.30	76.4	76.42			
C_{44} (GPa)	77.1	77.11	56.4	56.45			
c_{44} (GPa)	120.9	120.93	117.2	109.76			

	Silicon carbide						
	Expt.	DFT-LDA		TIII		EA	
	Ref.[m]	Ref.[d]	Ref.[c]	Ref.[n]	This paper	Ref.[a]	This paper
a_0 (Å)	4.3596	4.344	4.338	4.32	4.321	4.359	4.359
C_{11} (GPa)	390	390	405	420.0	436.63	382	383.78
C_{12} (GPa)	142	134	145	120.0	117.94	145	144.41
C_{44} (GPa)	256	253	247	260.0	256.60	240	239.75
c_{44} (GPa)		273	311.0	311.0	310.81	305	304.75

	Silicon dioxide						
	Expt.		DFT-LDA	DFT-GGA	BKS		
	Ref.[g]	Ref.[h]	Ref.[i]	Ref.[i]	Ref.[j]	This paper	
a_0 (Å)		4.914	4.8701	5.0284	4.941	4.942	
c_0 (Å)		5.405	5.3626	5.5120	5.405	5.448	
C_{11} (GPa)	85.9	86.6	76.6	87.1	90.5	90.59	
C_{12} (GPa)	7.16	6.74	5.88	−7.82	8.1	8.06	
C_{13} (GPa)	10.94	12.40	6.58	6.30	15.2	15.21	
C_{14} (GPa)	−17.66	−17.80	−17.8	−17.0	−17.6	−17.68	
C_{33} (GPa)	89.59	106.40	95.9	87.1	107.0	106.94	
C_{44} (GPa)	57.77	58.0	54.1	49.1	50.2	50.23	
C_{66} (GPa)	39.4		35.3	47.5		41.26	

[a]Reference [61]; [b]Reference [73]; [c]Reference [68]; [d]Reference [74]; [e]Reference [75]; [f]Reference [62]; [g]Reference [76]; [h]Reference [77]; [i]Reference [78]; [j]Reference [63]; [k]Reference [79]; [l]Reference [80]; [m]Reference [81]; [n]Reference [55].

improvement of the lattice constants and elastic properties of α-quartz compared to the original BKS potential [78,82–84], but defects, interfaces, phase boundaries, and other relevant properties are significantly improved [85,86].

B. Elastic coefficients at finite hydrostatic pressure

After validation of our approach at zero stress, we investigate the effect of hydrostatic pressure on the elastic properties. In Fig. 4, we show the pressure-dependent elastic coefficients for all investigated materials and interatomic potentials.

The vertical dashed lines mark zero hydrostatic pressure. For bond-order potentials under hydrostatic tension, we consider only the range of pressures where the first-neighbor shell is within the first cutoff distance, corresponding to Si–Si bond distances of $r_{Si,Si} = 2.7$ Å for KUM and TIII and $r_{Si,Si} = 2.75$ Å for EAII. For silicon carbide, this happens when the Si–C bond length exceeds $r_{Si,C} = 2.2$ Å. Under compression, we consider the full range of pressures to highlight the impact of second-nearest neighbors on the elastic properties. We first consider the elastic coefficients C_{ij}, which include the contribution from nonaffine displacements. The qualitative
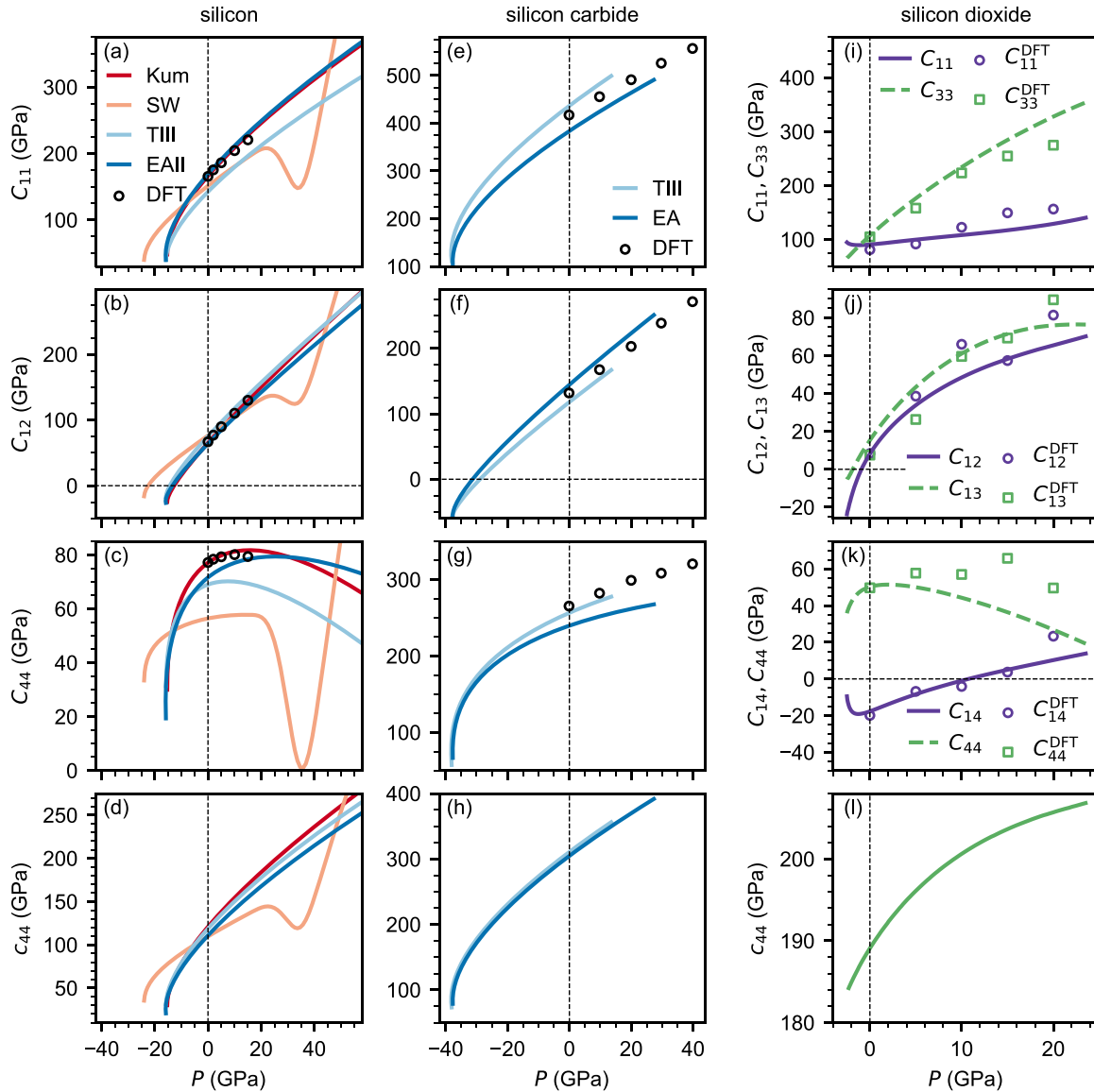
FIG. 4. Pressure-dependent elastic coefficients at zero temperature for silicon (a)–(d), silicon carbide (e)–(h), and silicon dioxide (i)–(l). DFT results for silicon are taken from Ref. [87], for silicon carbide from Ref. [88], and for silicon dioxide from Ref. [89]. C_{ij}: Elastic coefficients with nonaffine contributions. c_{ij}: Elastic coefficients without nonaffine contributions.

behavior of the elastic coefficients of pure silicon is similar for all bond-order potentials. Upon compression, C_{11} and C_{12} increase monotonically while C_{44} initially increases, reaches a maximum, and subsequently decreases. The location and the absolute value of that maximum varies slightly between the potentials. Under tension, all three elastic moduli decrease rapidly. In contrast, the pressure dependence of the elastic coefficients for the SW potential is qualitatively different from the one observed for the bond-order potentials. Under compression, all moduli increase up to a pressure of ≈ 24 GPa. At this point, second-nearest neighbors enter the cutoff range and are included in the interaction. Upon further compression, the elastic moduli as a function of pressure drops towards a local minimum before starting to increase rapidly. Under tension, the elastic moduli decrease, although the decrease is less rapid compared to the one seen for the bond-order potentials. We note that the effect of second-nearest neighbors

on the elastic properties is a common problem for interatomic potentials with a finite interaction range [25,69]. Nevertheless, the large effect in SW-like potentials at comparatively small compressive pressures has not been reported.

In the case of silicon dioxide, we present results only in the pressure range $-3\,\text{GPa} \leqslant P \leqslant 23\,\text{GPa}$. For smaller/larger pressures, the initial lattice becomes unstable and would undergo a phase transformation (as discussed below in Sec. V C) which results in a sudden change of the elastic coefficients. In the region where the initial crystalline structure of silicon dioxide is stable, the elastic coefficients, with the exception of C_{44}, increase with increasing compression. In contrast, during tension all elastic moduli, except C_{14}, decrease.

In Figs. 4(d), 4(h) and 4(l), we show the elastic modulus c_{44} without the contribution from nonaffine displacements. Due to symmetries in the lattice, the nonaffine contribution in silicon and silicon carbide enters only in C_{44}, while for
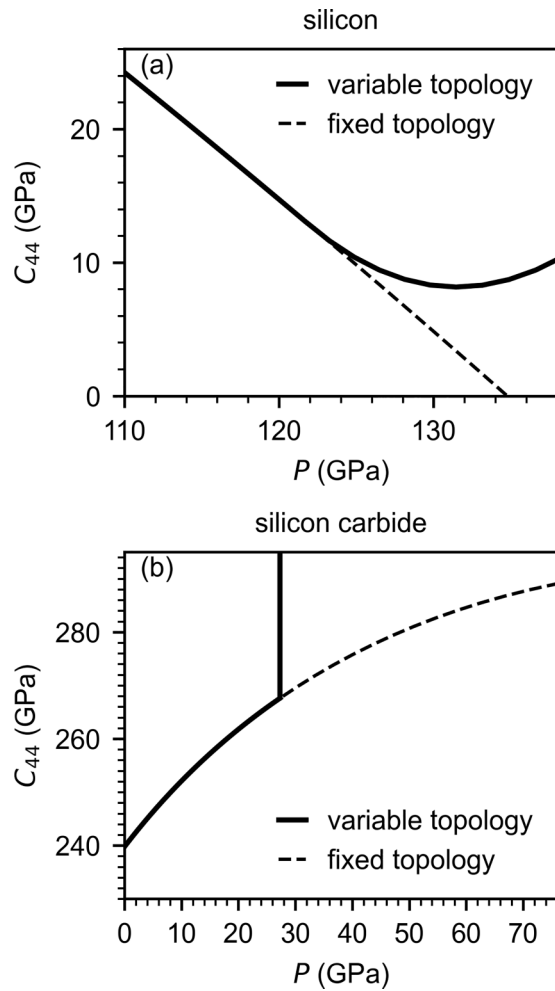
FIG. 5. Effect of a fixed bonding topology versus a variable topology on the pressure dependence of C_{44} for silicon (KUM) (a) and silicon carbide (EA) (b). The results deviate in regions where neighbors sit within the cutoff distance.

silicon dioxide the nonaffine contribution is nonzero for all elastic moduli. If we neglect the nonaffine contribution, the elastic modulus c_{44} increases continuously under compression and decreases less rapidly under tension. This behavior is independent of the material and the interatomic potential and is related to the stiffening of the effective pair interactions. In direct comparison with the C_{44} value, we observe that the nonaffine part generally decreases the elastic coefficients.

In the preceding paragraphs, we saw that the inclusion of second-nearest neighbors in some interatomic potentials affects the pressure dependent elastic coefficients in such a way that their behavior is no longer reliable. To check if this is also true for the other potentials, e.g., KUM, we perform additional simulations using the fixed topology approach described in Sec. IV. In Fig. 5, we show calculations of C_{44} at fixed and variable topologies. The figure shows that at a compressive pressure of ≈ 123 GPa, the elastic coefficient C_{44} for silicon [Fig. 5(a)] increases rapidly if a variable topology is used. (Note that we excluded those extreme pressures in the discussion above.) If we rather use a fixed bonding topology in the KUM potential, this increase disappears and the C_{44} curve

continuously drops to zero, where the lattice looses stability (as discussed in the next section). The reason for this sudden increase is once again the inclusion of second-nearest neighbors. The pressure for this to occur is a factor of five larger than what is observed for the SW potential, and is related to the smaller cutoff radius $r_c^{\text{KUM}} = 3.0$ Å $< r_c^{\text{SW}} = 3.77$ Å. The inclusion of second nearest-neighbors therefore effectively stabilizes the crystal lattice and the system avoids the elastic instability.

Figure 5(b) shows once more the pressure dependence of C_{44} for silicon carbide modeled using the EA potential. This time, we also show the effect of second-nearest neighbors on the pressure dependency of C_{44}. At the pressure where second-nearest neighbors enter the interaction range, C_{44} increases instantaneously. Using a fixed topology in the EA potential for silicon carbide does not change the pressure dependency of C_{44} and enables us to investigate the elastic coefficients for higher compressive pressures. In the following section, which discusses lattice stability, we will only show results for potentials with fixed topology since the lattices typically mechanically collapse beyond the cutoff range.

C. Stability of the crystal lattice under hydrostatic pressure

So far, we have assumed the initial crystal structure to remain stable under arbitrarily large deformation. However, as already discussed in Sec. II H, instabilities related to the h matrix or to atomic positions at fixed h matrix can occur. In the literature [13,42], they are referred to elastic and dynamic instability, respectively. We first focus on the elastic instability, which for cubic lattice symmetry reduces to the conditions [8,13,42],

$$M_1 = C_{11} + 2C_{12} \geqslant 0,$$
$$M_2 = C_{44} \geqslant 0,$$
$$M_3 = C_{11} - C_{12} \geqslant 0,$$

on the elastic coefficients for the lattice to be stable. For silicon dioxide with a trigonal lattice symmetry to become unstable, one of the following criteria needs to be violated [42]:

$$N_1 = C_{11} - |C_{12}| \geqslant 0,$$
$$N_2 = C_{44} \geqslant 0,$$
$$N_3 = C_{33}(C_{11} + C_{12}) - 2C_{13}^2 \geqslant 0,$$
$$N_4 = C_{44}(C_{11} - C_{12}) - 2C_{14}^2 \geqslant 0.$$

Here, M_1 to M_3 and N_1 to N_4 are the unique values of the eigenvalues of the tensor of elastic coefficients, some of which are degenerate. In Fig. 6, we show these eigenvalues together with the smallest eigenvalue of the Hessian.

In the following, we refer to the pressure at which one of the eigenvalues M_i, N_i, or λ_i, vanishes as a critical pressure, P^c. We first consider the behavior of pure silicon under hydrostatic compression using bond-order potentials. With increasing pressure, M_1 increases continuously while M_2 and M_3 decrease. Thereby, M_3 is the vanishing eigenvalue for the KUM+FT and the TIII+FT potential. M_3 vanishes at a critical pressure of $P^c \approx 125.7$ GPa and $P^c \approx 78.3$ GPa for
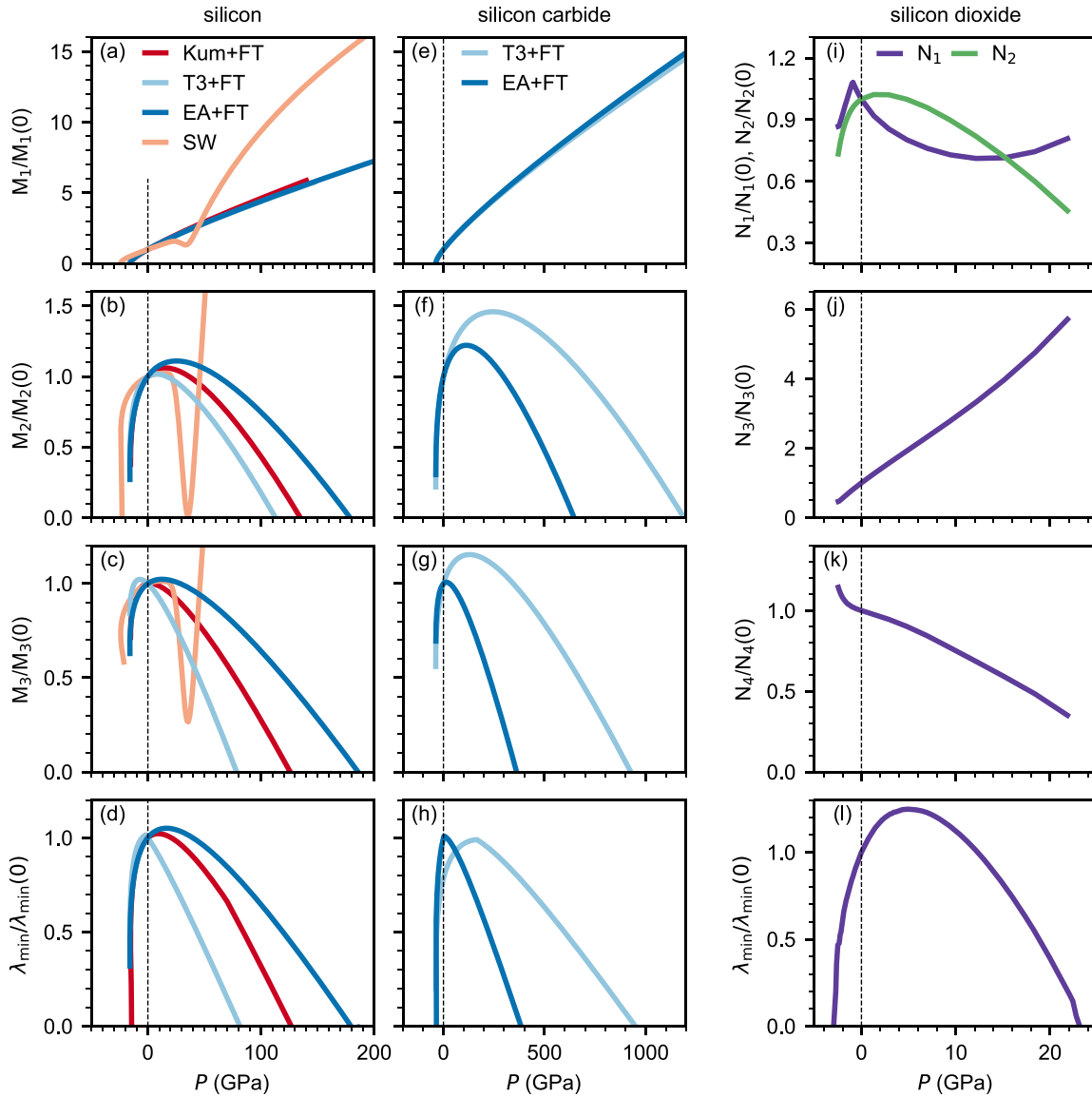
FIG. 6. Eigenvalues of the elastic tensor $\underline{\underline{C}}$, denoted by M_1, M_2, M_3 for cubic solids and N_1, N_2, N_3, N_4 for silicon dioxide, and smallest eigenvalue $\lambda_{\min}$ of the Hessian $\mathbb{H}$ as a function of pressure P. Shown are results for silicon (a)–(d), silicon carbide (e)–(h), and silicon dioxide (i)–(l). The eigenvalues are normalized to their value at zero hydrostatic pressure. The systems lose mechanical stability when an eigenvalue becomes negative.

the KUM+FT and the TIII+FT potential, respectively. Interestingly, for the EAII+FT potential M_2 vanishes first at a critical pressure of $P^c \approx 175.9$ GPa. TIII and EAII have the same functional form but their difference in critical pressure is significant. Using the SW potential, none of the stability criteria are violated under compression, but the eigenvalues M_1, M_2, and M_3 all have a minimum at a pressure ≈ 35.72 GPa. Under tension, M_1 vanishes for all bond-order potentials at an almost identical pressure of $P^c \approx -15$ GPa. For the SW potential, M_2 vanishes at $P^c \approx -22.7$ GPa. Comparing the critical pressures from an elastic instability with the ones from a dynamic instability, we observe that they occur at almost the same pressure.

For silicon carbide, which also has a cubic crystal structure, we observe that M_3 vanishes first in all interaction potentials. The critical pressures are $P^c \approx 949.4$ GPa for TIII+FT and

$P^c \approx 383.64$ GPa for EA+FT. Under dilatation, M_1, vanishes first at approximately $P^c \approx -38$ GPa for both potentials. We observe again that the critical pressure for the dynamic instability is in accordance with the one obtained from the elastic stability analysis.

For α-quartz, we observe dynamic instabilities at critical pressures of $P^c \approx 23.3$ GPa and $P^c \approx -2.94$ GPa for compression and tension. As a result of these dynamic instabilities, the initial crystalline structure becomes unstable and transforms to a new stable crystalline state. These phase transformations lead to an instantaneous change in the elastic coefficients for silicon dioxide and result in a sudden change of the elastic stability moduli N_i. Since the elastic stability conditions are finite $N_i > 0$ at the critical pressure for the dynamic instability, we conclude that the dynamic instability is responsible for these phase transformation.
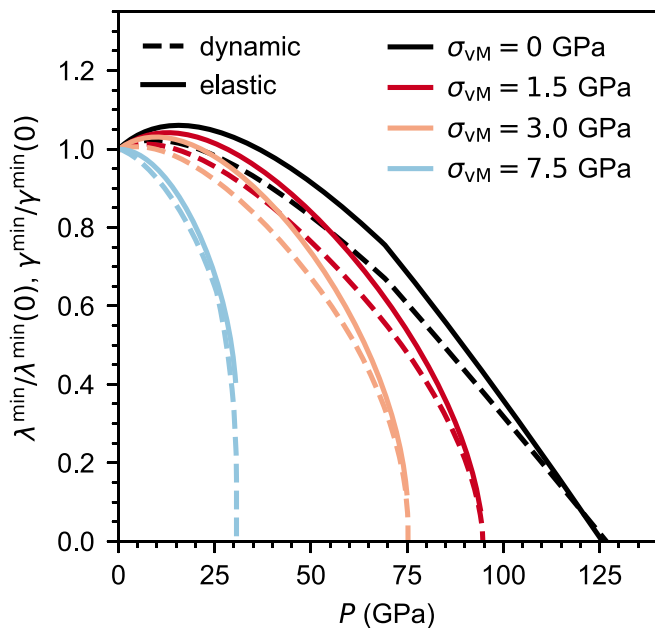
FIG. 7. Smallest eigenvalue γ^{min} of the elastic tensor $\underline{\underline{C}}^{\mathrm{sym}}$ and smallest eigenvalue λ^{min} of the Hessian $\mathbb{H}$ of diamond cubic silicon. The multiaxial stress state is triaxial compression, $\sigma_{xx} = \sigma_{yy} \neq \sigma_{zz}$, and $\sigma_{xy} = \sigma_{xz} = \sigma_{yz} = 0$.

D. Stability of the crystal lattice at multiaxial stress

Deformation of solids in real-world applications is rarely hydrostatic and instead complex multiaxial states of stress may arise. Real-world scenarios even exhibit gradients of the stress field, such as when contacting a surface with a sphere [90]. We here consider as an example a homogeneous multiaxial state of stress that may be representative for a volume element directly underneath the apex of a contacting sphere. Homogeneous multiaxial stresses are often used as models for shock compression (Hugoniot) experiments [91–94].

We consider diamond cubic silicon subjected to a prescribed stress tensor

$$\underline{\sigma} = \begin{pmatrix} -P - \sigma_{\mathrm{vM}}/3 & 0 & 0 \\ 0 & -P - \sigma_{\mathrm{vM}}/3 & 0 \\ 0 & 0 & -P + 2\sigma_{\mathrm{vM}}/3 \end{pmatrix},$$

where σ_{vM} is the von Mises stress. The loading is in the $\langle 100 \rangle$ direction. Stability of the same crystal loaded in a rotated frame will differ from the scenario presented in the following section.

The interaction between atoms is modeled using the KUM potential with a fixed cutoff for $\sigma_{\mathrm{vM}} \neq 0$ and the KUM+FT potential for $\sigma_{\mathrm{vM}} = 0$. To rule out the possible effects of the finite interaction range described above, we checked that the atoms interact only with nearest neighbors as long as the initial crystalline structure remains stable. In contrast to the previous subsections, the deformation of the box is induced by prescribing the stress tensor $\underline{\sigma}$ and allowing the simulation cell to fluctuate. The stability of the lattice is now determined by the symmetric part of the tensor of Birch coefficients C_{ij}^{sym}, which no longer has the original cubic symmetry because of the multiaxial stress state. In Fig. 7, we show the smallest eigenvalue γ^{min} of C_{ij}^{sym} together with the smallest eigenvalue

of the Hessian λ^{min} for certain values of σ_{vM}. All eigenvalues have been normalized to their value at the first step of deformation, and we consider only the range of pressures until one of the eigenvalues, λ^{min} or γ^{min}, becomes zero. We observe that the values of γ^{min} decrease with increasing compression, but always remain finite. In contrast, the eigenvalues of the Hessian become zero at some critical pressure P^{c}, marking a phase transition induced by a dynamic instability. Thereby, the critical pressure P^{c} for the phase transition decreases with increasing σ_{vM}, i.e., with increasing deviation from the purely hydrostatic stress state. Upon compressing the crystal above the critical pressure for the dynamic instability, the atoms instantaneously transform to a new stable crystalline structure, which here is the β-Sn (or Si-II) phase of silicon. This change in simulation cell and atomic position is accompanied by sudden changes in the vibrational and elastic properties.

VI. DISCUSSION

This paper establishes a consistent framework for the calculation of finite stress elastic coefficients in molecular RVEs, including the effect of nonaffine atomic displacements. It is important to reiterate that the elastic coefficients sensitively depend on the type of embedding medium. The literature [4–6,11–14,41,43,95,96] typically discussed elastic coefficients at constant second Piola-Kirchhoff stress or at constant Cauchy stress. The latter is also known as the Birch coefficients. However, even these situations are highly idealized as they ignore stress gradients in the embedding medium that cannot be avoided unless this medium itself is perfectly matched, i.e. it consists of repeated images of the RVE. This means that mechanical stability of the RVE depends on the type of embedding. Like most of the literature [13,14,70,87,89,97–101], we have restricted our example calculations to stability at constant Cauchy stress, but to what extend these calculations are representative of actual experimental conditions depends on the specific experiment.

Numerically, Hessians of RVEs are typically computed using finite differences. We have here also derived analytical expressions for complex many-body potentials that allow analytical computation of Hessians, vibrational modes, elastic coefficients, and other linear response properties. This enables calculation of these properties for large heterogeneous systems, where finite differences become prohibitive or are impossible, such as near an instability.

As example calculations, we applied this method to a set of crystals. All crystals under investigation show finite ranges of stability in experiments. For silicon, diamond anvil cell experiments show a collapse of the diamond cubic lattice into β-tin at 12.7 GPa [102]. This pressure roughly matches the equilibrium transition pressure obtained from a tangent construction to the pressure volume curves of the respective phases in molecular calculations (12.7 GPa TIII [70] 9.8 GPa KUM [103], 7.8 GPa DFT-LDA [70]). Our own calculations of the equilibrium diamond cubic to β-Sn transition show transition pressures between 11.8 and 13 GPa for the investigated interatomic potentials. The ultimate limit of lattice stability occurs at much higher pressures (125.7 GPa KUM, 78.3 GPa TIII, 175.9 GPa EAII).

For silicon-carbide, diamond anvil cell experiments with a pressure medium show an instability of 3C-SiC to a rocksalt structure at roughly 100 GPa [104]. DFT computations predict a slightly smaller critical pressure between $P^c \approx 58$ GPa and $P^c \approx 75$ GPa for this phase transition [100,105]. Again, the ultimate stability of 3C-SiC from our calculations is much higher (949.4 GPa TIII, 383.4 GPa EA). Consistent with DFT calculations [88], we find that a vanishing eigenvalue M_3 (tetragonal shear) leads to this instability. This is in contrast with results from Tang and Yip, who identified M_2 (simple shear) as the eigenvalue that vanishes first [97,98]. In general, care has to be taken specifically for SiC, which has a large number of polymorphs. Those polymorphs cannot be discriminated by the simple potentials used here that only consider nearest neighbor interactions. In addition, SiC shows significant charge transfer. A consideration of Coulombic interactions is likely necessary to capture the experimentally observed collapse to rocksalt, which is a prototypical ionic structure.

For silicon dioxide, a crystal-to-crystal phase transition is observed in diamond anvil cell experiments at a pressure of roughly 21 GPa [106]. These experiments are supported by numerical computations which predict a transition from α-quartz (quartz I) to quartz-II phase. Simulations predict the transition pressure to be between 16 GPa and 22 GPa, depending on the deviation from the purely hydrostatic stress state [99,107–109]. The experimental and computational estimated critical pressure agrees well with the dynamical instability $P^c \approx 23.3$ GPa in our simulations.

The ultimate stability of crystalline lattices (as characterized by a dynamical or elastic instability) appears to be reached in experiments on silicon dioxide but does not appear to play a role in the stability of silicon and silicon carbide. In particular, for silicon, the experimentally observed Si-I to Si-II transition appears where the high pressure phase becomes thermodynamically stable and not where the lattice collapses. Transitions between the two states must then involve nucleation and growth processes, as transitioning directly between two crystalline phases involves barriers that scale with sample volume.

However, there are multiple factors that lower the ultimate limit of stability as obtained from our zero-temperature calculations. First, temperature softens the elastic response and helps overcome energy barriers, which can significantly affect the critical pressure. For example, Mizushima *et al.* used finite temperature calculations to show that the critical pressure of lattice stability in silicon reduces from 105 GPa at zero temperature to 64 GPa at room temperature [70]. Second, it is difficult to achieve perfect hydrostatic conditions in diamond anvil cell experiments. For example, anvil cell experiments using ethanol-methanol as a pressure medium have been reported to deviate from a purely hydrostatic condition at around 10 GPa pressure [110,111]. Our calculations on silicon show that multiaxial stress significantly reduces the limit of lattice stability. As shown in Fig. 7, a shear stress of magnitude equal to 10% of the hydrostatic pressure reduces the critical pressure roughly by a factor of two. A similar trend was recently observed in boron carbide, where an additional shear stress significantly reduces the yield stress [112,113]. A combination of temperature fluctuations and multiaxiality therefore likely lowers the limit of lattice stability significantly, potentially to the pressure of the purely thermodynamic transition.

VII. SUMMARY AND CONCLUSIONS

In this paper, we revisited the question of how to define elastic coefficients at an arbitrary state of stress and included the role of nonaffine displacements. Based on these theoretical results, we gave closed-form expressions for a select set of many-body interatomic potentials for all terms required to analytically compute the elastic coefficients in atomistic simulations. These terms include expressions for the Hessian, the nonaffine forces, and the Born elastic coefficients for generic many-body potentials. These analytical expressions are implemented in our open-source software MATSCIPY [26] and they have the advantage of being exact. Their derivation is based on a generalized, unified functional form that fits many empirical interatomic potentials. It is easily extendable to interatomic potentials beyond those presented here. The resulting elastic properties are fast to compute and not prone to parameters in the numerical computation.

We demonstrated these methods on the elastic coefficients and the lattice stability of silicon, silicon carbide and silicon dioxide under volumetric and multiaxial deformation. We highlighted that all employed bond-order potentials and cluster potentials using a finite interaction range suffered from unreliable results once second-nearest neighbors had been included in the interaction range. Furthermore, we showed that multiaxiality plays a critical role in the stability limits of crystalline lattices.

ACKNOWLEDGMENTS

[1] N. C. Admal and E. B. Tadmor, A unified interpretation of stress in molecular systems, J. Elast. **100**, 63 (2010).

[2] N. C. Admal and E. B. Tadmor, The non-uniqueness of the atomistic stress tensor and its relationship to the generalized Beltrami representation, J. Mech. Phys. Solids **93**, 72 (2016).

[3] K. Huang, On the atomic theory of elasticity, Proc. R. Soc. London A **203**, 178 (1950).

[4] T. H. K. Barron and M. L. Klein, Second-order elastic constants of a solid under stress, Proc. Phys. Soc. **85**, 523 (1965).

[5] R. Thurston, Effective elastic coefficients for wave propagation in crystals under stress, J. Acoust. Soc. Am. **37**, 348 (1965).

[6] D. C. Wallace, Thermoelasticity of stressed materials and comparison of various elastic constants, Phys. Rev. **162**, 776 (1967).

[7] M. Born, Thermodynamics of crystals and melting, J. Chem. Phys. **7**, 591 (1939).

[8] M. Born, On the stability of crystal lattices, Math. Proc. Camb. Phil. Soc. **36**, 160 (1940).

[9] M. Born and K. Huang, *Dynamical Theory of Crystal Lattices* (Clarendon Press, Oxford, New York, 1954).

[10] D. C. Wallace, Thermoelastic theory of stressed crystals and higher-order elastic constants, Solid State Phys. **25**, 301 (1970).

[11] R. Hill, On the elasticity and stability of perfect crystals at finite strain, Math. Proc. Cambridge Philos. Soc. **77**, 225 (1975).

[12] R. Hill and F. Milstein, Principles of stability analysis of ideal crystals, Phys. Rev. B **15**, 3087 (1977).

[13] J. Wang, S. Yip, S. R. Phillpot, and D. Wolf, Crystal Instabilities at Finite Strain, Phys. Rev. Lett. **71**, 4182 (1993).

[14] J. Wang, J. Li, S. Yip, S. Phillpot, and D. Wolf, Mechanical instabilities of homogeneous crystals, Phys. Rev. B **52**, 12627 (1995).

[15] G. Grimvall, B. Magyari-Köpe, V. Ozoliņš, and K. A. Persson, Lattice instabilities in metallic elements, Rev. Mod. Phys. **84**, 945 (2012).

[16] C. S. G. Cousins, Inner elasticity, J. Phys. C: Solid State Phys. **11**, 4867 (1978).

[17] E. B. Tadmor and R. E. Miller, *Modeling Materials: Continuum, Atomistic and Multiscale Techniques* (Cambridge University Press, Cambridge, UK, 2011).

[18] J. R. Ray, Elastic constants and statistical ensembles in molecular dynamics, Comput. Phys. Rep. **8**, 109 (1988).

[19] J. Lutsko, Generalized expressions for the calculation of elastic constants by computer simulation, J. Appl. Phys. **65**, 2991 (1989).

[20] M. Tang and S. Yip, Atomistic simulation of thermomechanical properties of β-SiC, Phys. Rev. B **52**, 15150 (1995).

[21] A. Lemaître and C. Maloney, Sum rules for the quasi-static and visco-elastic response of disordered solids at zero temperature, J. Stat. Phys. **123**, 415 (2006).

[22] S. Karmakar, E. Lerner, and I. Procaccia, Athermal nonlinear elastic constants of amorphous solids, Phys. Rev. E **82**, 026105 (2010).

[23] B. Cui, A. Zaccone, and D. Rodney, Nonaffine lattice dynamics with the Ewald method reveals strongly nonaffine elasticity of α-quartz, J. Chem. Phys. **151**, 224509 (2019).

[24] M. Xiong, X. Zhao, N. Li, and H. Xu, General energy-strain scheme for accurate evaluation of the born elasticity term for solid and liquid systems under finite temperature and pressure conditions, Comput. Phys. Commun. **247**, 106940 (2020).

[25] M. H. Müser, S. V. Sukhomlinov, and L. Pastewka, Interatomic potentials: Achievements and challenges, Adv. Phys.: X **8**, 2093129 (2023).

[26] MATSCIPY: Materials science with Python at the atomic-scale.

[27] M. Parrinello and A. Rahman, Polymorphic transitions in single crystals: A new molecular dynamics method, J. Appl. Phys. **52**, 7182 (1981).

[28] W. M. Lai, D. H. Rubin, D. Rubin, and E. Krempl, *Introduction to Continuum Mechanics* (Butterworth-Heinemann, Waltham, MA, USA, 2009).

[29] H. C. Öttinger, *Beyond Equilibrium Thermodynamics* (Wiley-VCH, Hoboken, NJ, USA, 2005).

[30] R. E. Miller, E. B. Tadmor, J. S. Gibson, N. Bernstein, and F. Pavia, Molecular dynamics at constant Cauchy stress, J. Chem. Phys. **144**, 184107 (2016).

[31] M. A. Biot, *Mechanics of Incremental Deformations* (John Wiley & Sons, Inc., New York, London, Sydney, 1965).

[32] Ted Belytschko, Wing Kam Liu, Brian Moran, and Khalil Elkhodary (Wiley, 2014).

[33] F. Birch, Finite elastic strain of cubic crystals, Phys. Rev. **71**, 809 (1947).

[34] F. Birch, Elasticity and constitution of the Earth's interior, J. Geophys. Res. **57**, 227 (1952).

[35] R. S. Elliott, N. Triantafyllidis, and J. A. Shaw, Stability of crystalline solids—I: Continuum and atomic lattice considerations, J. Mech. Phys. Solids **54**, 161 (2006).

[36] S. M. Kozlov, Averaging of random operators, Math. USSR Sb. **37**, 167 (1980).

[37] G. C. Papanicolaou and S. R. S. Varadhan, Boundary value problems with rapidly oscillating random coefficients, Random fields (Esztergom, Hungary, 1979), Vol. II, edited by J. Fritz, J. L. Lebowitz, and D. Szász. Colloq. Math. Soc. János Bolyai 27, 835 (1981).

[38] A. Zaccone and E. Scossa-Romano, Approximate analytical description of the nonaffine response of amorphous solids, Phys. Rev. B **83**, 184205 (2011).

[39] D. Machon, F. Meersman, M. Wilding, M. Wilson, and P. McMillan, Pressure-induced amorphization and polyamorphism: Inorganic and biochemical systems, Prog. Mater. Sci. **61**, 216 (2014).

[40] J. Grießer, G. Moras, and L. Pastewka, Yielding under compression and the polyamorphic transition in silicon, Phys. Rev. Mater. **7**, 055601 (2023).

[41] D. C. Wallace and J. L. Patrick, Stability of crystal lattices, Phys. Rev. **137**, A152 (1965).

[42] F. Mouhat and F.-X. Coudert, Necessary and sufficient elastic stability conditions in various crystal systems, Phys. Rev. B **90**, 224104 (2014).

[43] H. Wang and M. Li, Unifying the criteria of elastic stability of solids, J. Phys.: Condens. Matter **24**, 245402 (2012).

[44] L. Bouëssel du Bourg, A. U. Ortiz, A. Boutin, and F.-X. Coudert, Thermal and mechanical stability of zeolitic imidazolate frameworks polymorphs, APL Mater. **2**, 124110 (2014).

[45] M. F. Thorpe, Continuous deformations in random networks, J. Non-Cryst. Solids **57**, 355 (1983).

[46] H. He and M. F. Thorpe, Elastic Properties of Glasses, Phys. Rev. Lett. **54**, 2107 (1985).

[47] J. C. Phillips and M. F. Thorpe, Constraint theory, vector percolation and glass formation, Solid State Commun. **53**, 699 (1985).

[48] A. Zaccone, Elastic deformations in covalent amorphous solids, Mod. Phys. Lett. B **27**, 1330002 (2013).

[49] A. E. Carlsson, Beyond pair potentials in elemental transition metals and semiconductors, *Solid State Physics*, Vol. 43 (Academic Press, Cambridge, MA, USA, 1990), pp. 1–91.

[50] D. Squire, A. Holt, and W. Hoover, Isothermal elastic constants for argon. theory and Monte Carlo calculations, Physica **42**, 388 (1969).

[51] P. Schöffel and M. H. Müser, Elastic constants of quantum solids by path integral simulations, Phys. Rev. B **63**, 224108 (2001).

[52] G. C. Abell, Empirical chemical pseudopotential theory of molecular and metallic bonding, Phys. Rev. B **31**, 6184 (1985).

[53] J. Tersoff, New Empirical Model for the Structural Properties of Silicon, Phys. Rev. Lett. **56**, 632 (1986).

[54] D. W. Brenner, Empirical potential for hydrocarbons for use in simulating chemical vapor deposition of diamond films, Phys. Rev. B **42**, 9458 (1990).

[55] J. Tersoff, Modeling solid-state chemistry: Interatomic potentials for multicomponent systems, Phys. Rev. B **39**, 5566 (1989).

[56] F. H. Stillinger and T. A. Weber, Computer simulation of local order in condensed phases of silicon, Phys. Rev. B **31**, 5262 (1985).

[57] B. Jalali and S. Fathpour, Silicon photonics, J. Lightwave Technol. **24**, 4600 (2006).

[58] T. Kimoto and J. A. Cooper, *Fundamentals of Silicon Carbide Technology: Growth, Characterization, Devices and Applications* (John Wiley & Sons, Singapore, 2014).

[59] X. She, A. Q. Huang, O. Lucia, and B. Ozpineci, Review of silicon carbide power devices and their applications, IEEE Trans. Ind. Electron. **64**, 8193 (2017).

[60] P. J. Heaney, C. T. Prewitt, and G. V. Gibbs, *Silica: Physical Behavior, Geochemistry, and Materials Applications* (De Gruyter, Berlin, Boston, 2018).

[61] P. Erhart and K. Albe, Analytical potential for atomistic simulations of silicon, carbon, and silicon carbide, Phys. Rev. B **71**, 035211 (2005).

[62] T. Kumagai, S. Izumi, S. Hara, and S. Sakai, Development of bond-order potentials that can reproduce the elastic constants and melting point of silicon for classical molecular dynamics simulation, Comput. Mater. Sci. **39**, 457 (2007).

[63] B. W. H. van Beest, G. J. Kramer, and R. A. van Santen, Force Fields for Silicas and Aluminophosphates Based on *ab initio* Calculations, Phys. Rev. Lett. **64**, 1955 (1990).

[64] P. P. Ewald, The calculation of optical and electrostatic lattice potentials, Ann. Phys. **369**, 253 (1921).

[65] A. Y. Toukmaji and J. A. Board Jr., Ewald summation techniques in perspective: A survey, Comput. Phys. Commun. **95**, 73 (1996).

[66] M. I. Baskes, J. E. Angelo, and C. L. Bisson, Atomistic calculations of composite interfaces, Modell. Simul. Mater. Sci. Eng. **2**, 505 (1994).

[67] L. Pastewka, P. Pou, R. Pérez, P. Gumbsch, and M. Moseler, Describing bond-breaking processes by reactive potentials: Importance of an environment-dependent interaction range, Phys. Rev. B **78**, 161402(R) (2008).

[68] L. Pastewka, A. Klemenz, P. Gumbsch, and M. Moseler, Screened empirical bond-order potentials for Si-C, Phys. Rev. B **87**, 205410 (2013).

[69] M. H. Müser, Improved cutoff functions for short-range potentials and the Wolf summation, Mol. Simul. **48**, 1393 (2022).

[70] K. Mizushima, S. Yip, and E. Kaxiras, Ideal crystal stability and pressure-induced phase transition in silicon, Phys. Rev. B **50**, 14952 (1994).

[71] W. Voigt, *Lehrbuch der Kristallphysik* (B. G. Teubner, Leipzig, Berlin, 1910).

[72] J. F. Nye, *Physical Properties of Crystals: Their Representation by Tensors and Matrices* (Clarendon Press, Oxford, UK, 1957).

[73] W. M. Haynes, *CRC Handbook of Chemistry and Physics* (CRC Press, Boca Raton, FL, USA, 2016).

[74] K. Karch, P. Pavone, W. Windl, O. Schütt, and D. Strauch, *Ab initio* calculation of structural and lattice-dynamical properties of silicon carbide, Phys. Rev. B **50**, 17054 (1994).

[75] H. Balamane, T. Halicioglu, and W. A. Tiller, Comparative study of silicon empirical interatomic potentials, Phys. Rev. B **46**, 2250 (1992).

[76] E. Gregoryanz, R. J. Hemley, H. Mao, and P. Gillet, High-Pressure Elasticity of α-Quartz: Instability and Ferroelastic Transition, Phys. Rev. Lett. **84**, 3117 (2000).

[77] J. Wang, Z. Mao, F. Jiang, and T. S. Duffy, Elasticity of single-crystal quartz to 10 GPa, Phys. Chem. Miner. **42**, 203 (2015).

[78] J. Kermode, S. Cereda, P. Tangney, and A. De Vita, A first principles based polarizable O(N) interatomic force field for bulk silica, J. Chem. Phys. **133**, 094102 (2010).

[79] O. H. Nielsen and R. M. Martin, Stresses in semiconductors: *Ab initio* calculations on Si, Ge, and GaAs, Phys. Rev. B **32**, 3792 (1985).

[80] G. P. Purja Pun and Y. Mishin, Optimized interatomic potential for silicon and its application to thermal stability of silicene, Phys. Rev. B **95**, 224103 (2017).

[81] W. R. L. Lambrecht, B. Segall, M. Methfessel, and M. van Schilfgaarde, Calculated elastic constants and deformation potentials of cubic SiC, Phys. Rev. B **44**, 3685 (1991).

[82] A. Carre, J. Horbach, S. Ispas, and W. Kob, New fitting scheme to obtain effective potential from Car-Parrinello molecular-dynamics simulations: Application to silica, Europhys. Lett. **82**, 17001 (2008).

[83] T.-R. Shan, B. D. Devine, J. M. Hawkins, A. Asthagiri, S. R. Phillpot, S. B. Sinnott *et al.*, Second-generation charge-optimized many-body potential for Si/SiO$_2$ and amorphous silica, Phys. Rev. B **82**, 235302 (2010).

[84] E. Lee, K.-R. Lee, M. I. Baskes, and B.-J. Lee, A modified embedded-atom method interatomic potential for ionic systems, Phys. Rev. B **93**, 144110 (2016).

[85] D. Herzbach, K. Binder, and M. H. Müser, Comparison of model potentials for molecular-dynamics simulations of silica, J. Chem. Phys. **123**, 124711 (2005).

[86] L. C. Erhard, J. Rohrer, K. Albe, and V. L. Deringer, A machine-learned interatomic potential for silica and its relation to empirical models, npj Comput. Mater. **8**, 90 (2022).

[87] B. Karki, G. Ackland, and J. Crain, Elastic instabilities in crystals from *ab initio* stress-strain relations, J. Phys.: Condens. Matter **9**, 8579 (1997).

[88] Y.-P. Lu, D.-W. He, J. Zhu, and X.-D. Yang, First-principles study of pressure-induced phase transition in silicon carbide, Phys. B: Condens. Matter **403**, 3543 (2008).

[89] H. Kimizuka, S. Ogata, J. Li, and Y. Shibutani, Complete set of elastic constants of α-quartz at high pressure: A first-principles study, Phys. Rev. B **75**, 054109 (2007).

[90] K. L. Johnson, *Contact Mechanics* (Cambridge University Press, Cambridge, New York, 1985).

[91] J. N. Johnson, Shock propagation produced by planar impact in linearly elastic anisotropic media, J. Appl. Phys. **42**, 5522 (1971).

[92] R. Ravelo, T. C. Germann, O. Guerrero, Q. An, and B. L. Holian, Shock-induced plasticity in tantalum single crystals: Interatomic potentials and large-scale molecular-dynamics simulations, Phys. Rev. B **88**, 134101 (2013).

[93] Y. Fu, J. Michopoulos, and J.-H. Song, Dynamics response of polyethylene polymer nanocomposites to shock wave loading, J. Polym. Sci. Part B: Polym. Phys. **53**, 1292 (2015).

[94] T. C. O'Connor, R. M. Elder, Y. R. Sliozberg, T. W. Sirk, J. W. Andzelm, and M. O. Robbins, Molecular origins of anisotropic shock propagation in crystalline and amorphous polyethylene, Phys. Rev. Mater. **2**, 035601 (2018).

[95] G. Leibfried and W. Ludwig, Theory of anharmonic effects in crystals, Solid State Phys. **12**, 275 (1961).

[96] V. I. Levitas, Nonlinear elasticity of prestressed single crystals at high pressure and various elastic moduli, Phys. Rev. B **104**, 214105 (2021).

[97] M. Tang and S. Yip, Lattice instability in β-SiC and simulation of brittle fracture, J. Appl. Phys. **76**, 2719 (1994).

[98] M. Tang and S. Yip, Atomic Size Effects in Pressure-Induced Amorphization of a Binary Covalent Lattice, Phys. Rev. Lett. **75**, 2738 (1995).

[99] N. Choudhury and S. L. Chaplot, *Ab initio* studies of phonon softening and high-pressure phase transitions of α-quartz SiO$_2$, Phys. Rev. B **73**, 094304 (2006).

[100] W. Lee and X. Yao, First principle investigation of phase transition and thermodynamic properties of SiC, Comput. Mater. Sci. **106**, 76 (2015).

[101] V. I. Levitas, H. Chen, and L. Xiong, Lattice instability during phase transformations under multiaxial stress: Modified transformation work criterion, Phys. Rev. B **96**, 054118 (2017).

[102] B. Haberl, M. Guthrie, D. Sprouster, J. Williams, and J. Bradby, New insight into pressure-induced phase transitions of amorphous silicon: The role of impurities, J. Appl. Crystallogr. **46**, 758 (2013).

[103] G. Moras, A. Klemenz, T. Reichenbach, A. Gola, H. Uetsuka, M. Moseler, and L. Pastewka, Shear melting of silicon and diamond and the disappearance of the polyamorphic transition under shear, Phys. Rev. Mater. **2**, 083601 (2018).

[104] M. Yoshida, A. Onodera, M. Ueno, K. Takemura, and O. Shimomura, Pressure-induced phase transition in SiC, Phys. Rev. B **48**, 10587 (1993).

[105] K. Daviau and K. K. Lee, High-pressure, high-temperature behavior of silicon carbide: A review, Crystals **8**, 217 (2018).

[106] K. J. Kingma, R. J. Hemley, H.-k. Mao, and D. R. Veblen, New High-Pressure Transformation in α-Quartz, Phys. Rev. Lett. **70**, 3927 (1993).

[107] G. W. Watson and S. C. Parker, Dynamical instabilities in α-quartz and α-berlinite: A mechanism for amorphization, Phys. Rev. B **52**, 13306 (1995).

[108] J. S. Tse, D. D. Klug, Y. Le Page, and M. Bernasconi, High-pressure four-coordinated structure of SiO$_2$, Phys. Rev. B **56**, 10878 (1997).

[109] C. Campañá, M. H. Müser, J. S. Tse, D. Herzbach, and P. Schöffel, Irreversibility of the pressure-induced phase transition of quartz and the relation between three hypothetical post-quartz phases, Phys. Rev. B **70**, 224101 (2004).

[110] R. J. Angel, M. Bujak, J. Zhao, G. D. Gatta, and S. D. Jacobsen, Effective hydrostatic limits of pressure media for high-pressure crystallographic studies, J. Appl. Crystallogr. **40**, 26 (2007).

[111] K. Takemura, Hydrostaticity in high pressure experiments: Some general observations and guidelines for high pressure experimenters, High Press. Res. **41**, 155 (2021).

[112] J. D. Clayton, Towards a nonlinear elastic representation of finite compression and instability of boron carbide ceramic, Philos. Mag. **92**, 2860 (2012).

[113] D. E. Taylor, J. W. McCauley, and T. W. Wright, The effects of stoichiometry on the mechanical properties of icosahedral boron carbide under loading, J. Phys.: Condens. Matter **24**, 505402 (2012).

[114] A. Hjorth Larsen, J. J. Mortensen, J. Blomqvist, I. E. Castelli, R. Christensen, M. Dułak, J. Friis, M. N. Groves, B. Hammer, C. Hargus, E. D. Hermes, P. C. Jennings, P. Bjerre Jensen, J. Kermode, J. R. Kitchin, E. Leonhard Kolsbjerg, J. Kubal, K. Kaasbjerg, S. Lysgaard, J. Bergmann Maronsson *et al.*, The atomic simulation environment-a Python library for working with atoms, J. Phys.: Condens. Matter **29**, 273002 (2017).